

LASER INTERFEROMETER GRAVITATIONAL WAVE OBSERVATORY
- LIGO -
CALIFORNIA INSTITUTE OF TECHNOLOGY
MASSACHUSETTS INSTITUTE OF TECHNOLOGY

Technical Note	LIGO-T1900761-v4	02/12/2020
Design Requirement Document for Balanced Homodyne Readout of the 40m Prototype Interferometer		
Jonathan Richardson, Gautam Venugopalan, Yehonathan Drori, Hang Yu, Shruti Maliakal, Aaron Markowitz, Koji Arai, Rana Adhikari		

This is an internal working
note of the LIGO project.

California Institute of Technology
LIGO Project, MS 100-36
Pasadena, CA 91125
Phone (626) 395-2129
Fax (626) 304-9834
E-mail: info@ligo.caltech.edu

Massachusetts Institute of Technology
LIGO Project, Room NW22-295
Cambridge, MA 02139
Phone (617) 253-4824
Fax (617) 253-7014
E-mail: info@ligo.mit.edu

LIGO Hanford Observatory
P.O. Box 159
Richland, WA 99352
Phone (509) 372-8106
Fax (509) 372-8137
E-mail: info@ligo.caltech.edu

LIGO Livingston Observatory
19100 LIGO Lane
Livingston, LA 70754
Phone (225) 686-3100
Fax (225) 686-7189
E-mail: info@ligo.caltech.edu

WWW: <http://www.ligo.caltech.edu/>

Contents

1	Executive summary	4
2	Overview	6
3	Fuctional requirements	8
3.1	Length degrees of freedom	8
3.1.1	Digital gain setpoint	8
3.1.2	Homodyne angle	8
3.2	Mode Matching	11
3.3	Angular degrees of freedom	11
3.3.1	BHD board internal alignment	11
3.3.2	Aligning the LO/AS beams to the OMC board	15
4	Performance requirements	20
5	Local oscillator requirements	20
5.1	Relative intensity noise	20
5.2	Phase noise	21
5.2.1	Seismic isolation of relay optics	21
5.2.2	Actuator noise	25
6	Output mode cleaner requirements	27
6.1	Functions of the OMC cavity	27
6.1.1	Spectrum of input mode content	27
6.1.2	Cavity round-trip length	28
6.1.3	Higher order modes	28
6.2	Finesse	29
6.2.1	Required balancing between OMCs	29
6.3	Length noise	29
6.4	Angular (pointing) noise	32
6.4.1	Angular noise estimation	32
6.4.2	Simulation result	32
6.5	OMC thermal noise	34
6.5.1	Coating Brownian motion	35
6.5.2	Substrate/breadboard/PZT Brownian motion	36
7	Backscattered light requirements	36
7.1	Direct backscatter	37
7.2	OMC backscatter	38
8	Downstream loss requirements	39
8.1	Photodiode quantum efficiency	40
8.2	Output Faraday isolator	40
8.3	Super-polished HR routing mirrors	40
8.4	OMC losses	40

8.5	Mode-matching losses	40
9	Beamsplitter requirements	41
9.1	Transmittance-reflectivity balancing	41
9.2	Seismic isolation	41
10	Photodetector requirements	43
10.1	Amplifier noise	43
10.2	Transimpedance gain	43
10.3	Transimpedance gain balancing	44
A	Interferometer contrast defect	45
A.1	Definitions	45
A.2	DC analysis	45
B	OMC optical layout	51
C	40m ponderomotive squeezing	53
C.1	Beamsplitter imbalance analytic calculation	53
D	40m BHD testing plan	55
D.1	Lock acquisition	55
D.2	Noise couplings	56
D.3	Other tests	57
	Acronyms	59

1 Executive summary

This note considers the design requirements for implementation of [Balanced Homodyne Readout \(BHD\)](#) in the 40m prototype interferometer. The scope of this document is to describe the functional and performance requirements. The main conclusions that emerge from this work are summarized in [Table 1](#). In this table and throughout, we follow the convention used in [\[1\]](#) for references to the homodyne angle (i.e., $\zeta = 0^\circ$ corresponds to the phase quadrature).

The primary goal of this experiment is to test the adequacy of the [BHD](#) implementation planned for A+. Accordingly, phase quadrature readout is the main case of interest. However, a secondary scientific goal of the 40m is to achieve the direct observation of ponderomotive squeezing in a large-scale interferometer. Because the technical noise of the interferometer is expected to be lowest in a quadrature near the amplitude quadrature, we also quote the design requirements for readout of this quadrature. This case is discussed in [Appendix C](#).

	Requirement	Nominal ($\zeta = 0^\circ$)	Squeezing ($\zeta = 88^\circ$)	Refer to
OMC	Cavity finesse	400 ± 5	400 ± 5	Section 6.2
	RoC of CM1/CM2 [m]	2.575 ± 0.010	2.575 ± 0.010	Figure 18b
	Round trip length [m]	0.875 ± 0.010	0.875 ± 0.010	Figure 18c
	Angle of incidence [$^\circ$]	4.0 ± 0.5	4.0 ± 0.5	Appendix B
	Homodyne BS reflectivity [%]	50 ± 10	Appendix C	Section 9.1
	Length noise at 100 Hz [$\text{m}/\sqrt{\text{Hz}}$]	$\leq 1.3 \times 10^{-12}$	$\leq 1.6 \times 10^{-12}$	Figure 19b
	Thermal noise at 100 Hz [$\text{m}/\sqrt{\text{Hz}}$]	2.5×10^{-17}	2.5×10^{-17}	Figure 22
	Angular noise at 100 Hz [$\mu\text{rad}/\sqrt{\text{Hz}}$]	Nonexistent	Nonexistent	Section 6.4
LO	RIN [$1/\sqrt{\text{Hz}}$]	$\leq 1.0 \times 10^{-6}$	$\leq 2.0 \times 10^{-9}$	Figure 12
	Phase noise [$\text{rad}/\sqrt{\text{Hz}}$]	$\leq 1.0 \times 10^{-9}$	$\leq 2.8 \times 10^{-8}$	Figure 13
Optical losses	Photodiode QE [%]	≤ 2	≤ 2	Section 8.1
	OFI transmission [%]	≤ 2	≤ 2	Section 8.2
	Relay optic transmittance [%]	≤ 1	≤ 1	Section 8.3
	OMC transmission [%]	≤ 2	≤ 2	Section 8.4
	Mode-mismatch to OMC [%]	≤ 3	≤ 3	Section 8.5
PD	Amplifier noise (input-ref.) [$\text{A}/\sqrt{\text{Hz}}$]	$\leq 8.0 \times 10^{-12}$	$\leq 8.0 \times 10^{-12}$	Section 10.1
	Transimpedance gain [Ω]	≥ 260	≥ 260	Section 10.2
	Transimpedance balancing [%]	$\leq 8.0\%$	Appendix C	Section 10.3
Scatter	Arm cavity backscatter fraction	$\leq 10^{-21}$	$\leq 10^{-21}$	Figure 25
	OMC backscatter fraction [ppm]	≤ 5	≤ 5	Figure 26
	OFI isolation [dB]	≥ 30	≥ 30	See [2]

Table 1: Overall requirements for BHD assuming 100 mW of Local Oscillator (LO) power and 1 mW of defect carrier power. The “Nominal” column corresponds to phase quadrature readout ($\zeta = 0^\circ$). The “Squeezing” column corresponds to readout near the amplitude quadrature ($\zeta = 88^\circ$). This case is relevant for a secondary ponderomotive squeezing experiment planned at the 40m (see Appendix C).

2 Overview

The goal of this note is to inform the noise requirements on a proposed **BHD** experiment at the Caltech 40m interferometer, which is a prototype of the implementation planned for A+. At the time of writing, the optical topology of the 40m does not allow the **BHD** readout scheme to be implemented readily. Therefore, one objective of the design study is to arrive at a feasible optical layout, subject to the constraints imposed by the core interferometer optics and the existing vacuum envelope. One candidate layout is shown in Figure 1.

Some questions that have to be answered include:

1. Where should the **LO** beam be picked off from?
2. Where should the **BHD** system be installed? Depending on this, the isolation provided by suspensions used to route the beam from the pickoff point to the **BHD** setup will have to satisfy the **Relative Intensity Noise (RIN)** and phase noise requirements on the **LO** field.
3. Will the chosen optical layout allow sufficient attenuation of scattered light (i.e. Faraday isolator(s) + baffling) such that the interferometer sensitivity is not degraded?

A second objective of the design study that is analyzed in parallel deals with the design of two **Output Mode Cleaner (OMC)** cavities. The functions of the **OMC** cavities are (i) to strip the light incident on the **BHD DC Photo-Detectors (DCPD)** of **Radio Frequency (RF)** sidebands, (ii) maintain high transmission of the TEM00 mode of the carrier field, and (iii) provide sufficient attenuation of **Higher Order Modes (HOMs)**.

The questions we seek to answer are:

1. What should the geometry (round-trip length of the cavity and **Radius of Curvature (RoC)** of the curved mirrors) be such that sufficient attenuation of the **HOMs** is realized?
2. What should the **OMC** finesse be? For a chosen finesse, can sufficient attenuation of the **HOMs** be realized?
3. What kind of suspension system is required for the **OMC**? Will a modified **Vacuum Optical Parametric Oscillator (VOPO)** style suspension suffice?
4. Can the chosen beam routing strategy mode-match the **LO** beam to the **OMC** cavity eigenmode using a reasonable mode-matching telescope?
5. Is the direct backscatter for the chosen angle of incidence compatible with requirements?
6. What angular control is required to not degrade sensitivity?
7. What are the requirements on the various sources of thermal noise in the **OMC** cavities?

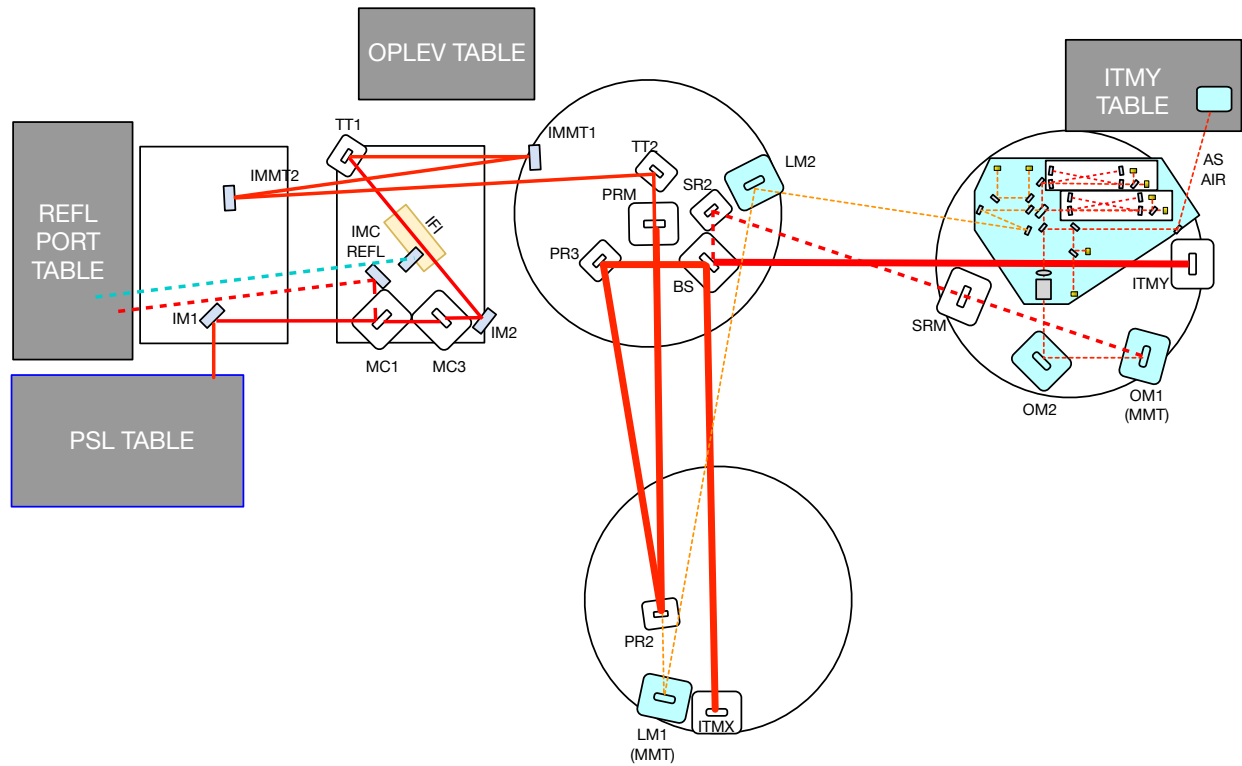


Figure 1: Proposed optical layout for the 40m BHD experiment. Only the vertex area optics are shown. Auxiliary beams, such as those associated with the Arm Length Stabilization (ALS) system and Optical Lever (Oplev) system are not shown.

3 Fuctional requirements

The system must provide the overall function of balanced homodyne detection. To achieve this functionality, the system must provide the following:

1. A stable **LO** beam picked off from the interferometer beam and delivered to the homodyne beamsplitter for recombination with the interferometer output field.
2. Vibration isolation for the components which form the **BHD** system (i.e. the relay suspensions and the **BHD** board suspension).
3. Output mode cleaning so that the unwanted **RF** sidebands and carrier higher-order modes are removed from the recombined beams.
4. Control capability for the necessary length degrees of freedom: the homodyne phase and the lengths of the two **OMC** cavities.
5. Control capability for the necessary angular degrees of freedom: the alignment of the two beams at the homodyne beamsplitter and the input alignment to the two **OMCs**.
6. Capability to realize sufficient mode-matching between the beams and to the **OMCs**.

Examples of the **BHD Instrument Sensing and Control (ISC)** schemes are discussed by H. Yu [3].

3.1 Length degrees of freedom

3.1.1 Digital gain setpoint

There will be 4 DC PDs in total to achieve, two after each OMC (OMC1 and OMC2). The SUM channel is formed by summing the PDs' output together, whereas the DIFF channel is formed by subtracting the PDs after OMC2 from those after OMC1. The DARM signal should show up only in the DIFF channel. In order to have a DARM readout, we need to first balance the digital gains of different DC PDs. Here we focus on balancing the gains of the PDs after OMC1 to those after OMC2.

This can be done by dithering DARM and tune the gains so that the DARM signal is zeroed in the SUM channel. This is shown in Figure 2

3.1.2 Homodyne angle

We consider here both the signal to set the DC ($\lesssim 0.1$ Hz) locking point of the homodyne angle ζ , and the signals can be used to stabilize the AC fluctuation of ζ in case > 0.1 Hz active control is needed.

To set the DC locking point, we can first dither DARM in length. When the homodyne angle ζ is properly set, this dithering signal should be maximized and therefore there is no first order sensitivity to ζ . To overcome this, we need to also dither the LO field and then look at the beat-notes between the two dithering signals. This is demonstrated in Figure 3. Since both signals are audio sidebands of the main carrier field, they will see the same mode content as the carrier and should thus have small offsets.

Double dithering scheme can only be used to provide the DC points with very low control bandwidth. If active feedback is required in the $0.1 - 10$ Hz band, we need to blend it with

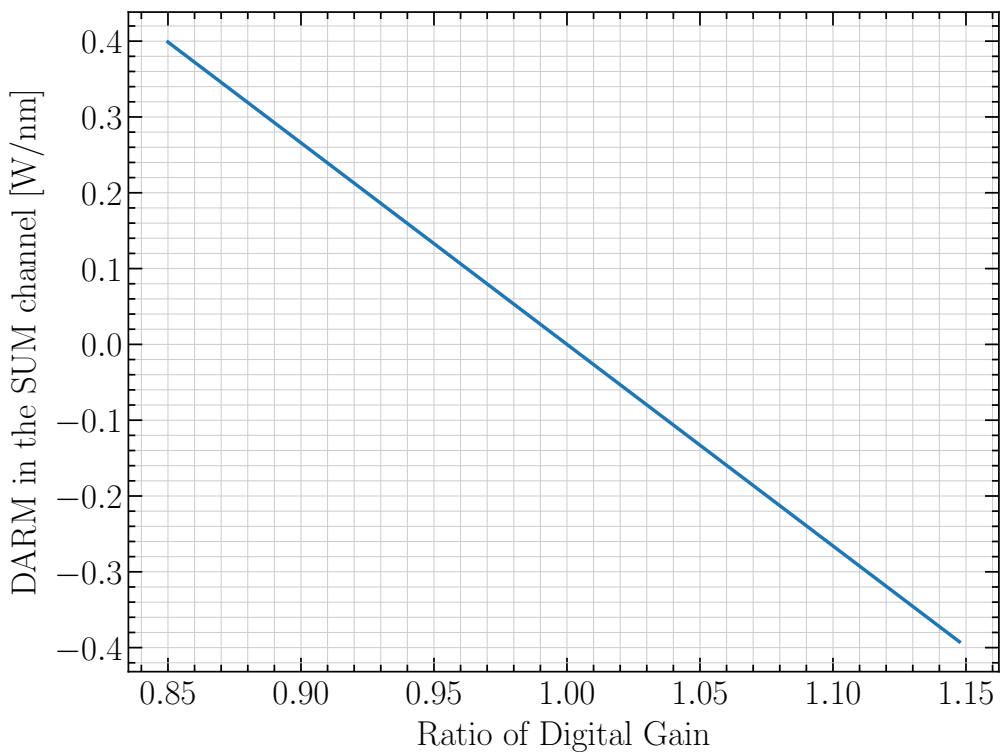


Figure 2: Set the digital gain by dither DARM and zero the signal in the SUM channel.

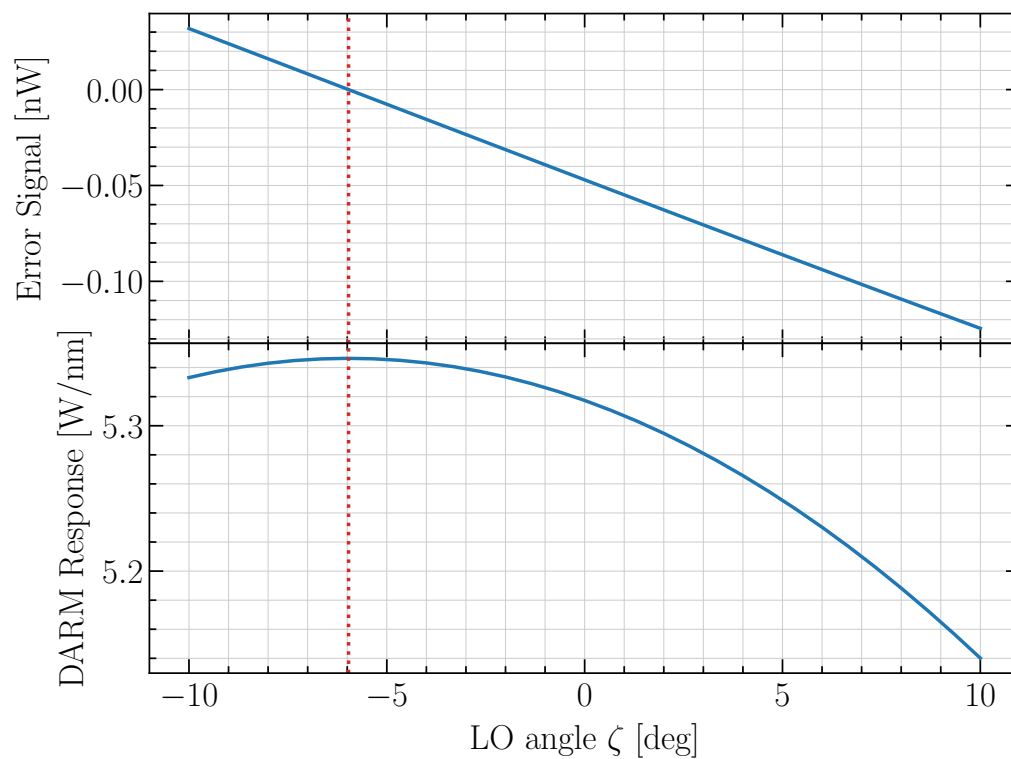


Figure 3: Top panel: error signal of the double-dithering scheme (i.e., dither both DARM and the LO and demodulate at the beatnote frequency). Bottom: DARM optical response. When the error signal

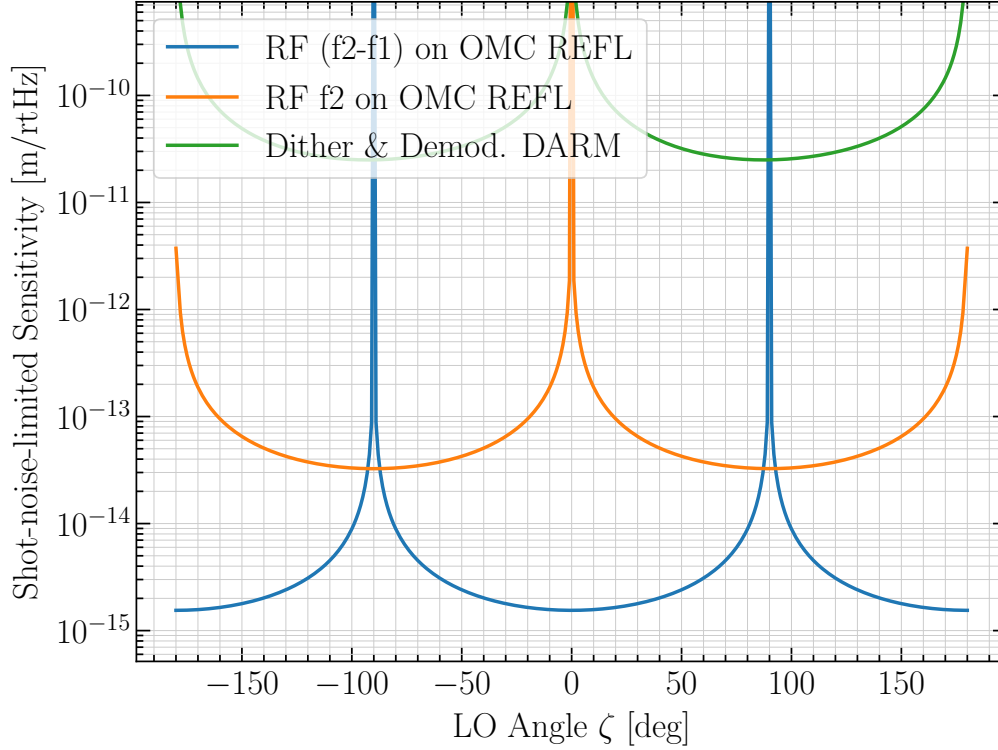


Figure 4: Shot-noise-limited sensitivity on the homodyne phase ζ as a function of ζ .

other signals. The most promising candidate is the (f_2-f_1) RF signal readout at the reflection of the OMC. One RF PD would be sufficient for this task as we only AC-couple the RF signal (note that the LO contains both f_1 and f_2 fields and would thus offset the error point of the (f_2-f_1) signal if only one RF PD is used.)

In Figure 4 we show the sensitivity of different schemes as a function of ζ .

3.2 Mode Matching

3.3 Angular degrees of freedom

3.3.1 BHD board internal alignment

We would like to have the two OMCs and the homodyne beamsplitter rigidly mounted to a single board. No active control is assumed for this setup, so here we derive the tolerances on the internal misalignments.

In Figure 7 we show how the power build-up as a function of misalignment. In the numerical simulation we have fixed the OMC 2 to be perfectly aligned while allow one of the mirrors of OMC 1 or the homodyne beamsplitter to be misaligned. The ratio of the transmitted power from the two OMCs thus tells as the fractional power build-up. In the mounting process, we expect to be able to reach 99.5% of the designed power. Thus the internal misalignment for each component is on the order of $10 \mu\text{rad}$.

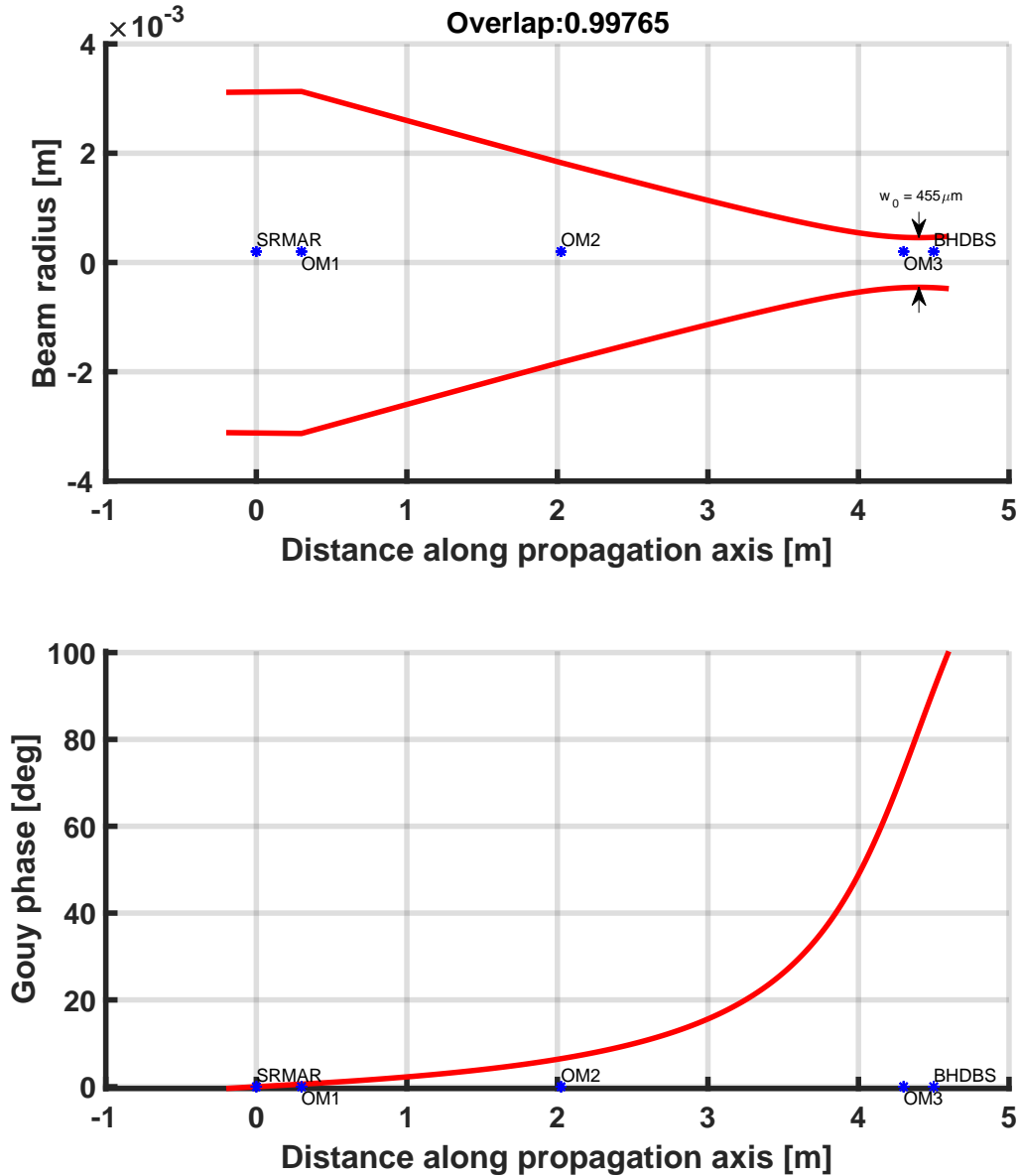


Figure 5: Mode-matching telescope for the AS beam (from SRM AR surface to the OMC input coupler). Here we have assumed the BHD BS is 4.5 m away from the SRM AR surface. We have ignored the beam propagation from the BHD BS to OMC input coupler, and required the last mirror to be at least 20 cm away from the OMC. In the calculation, OM1 and OM2 are curved whereas OM3 is flat.

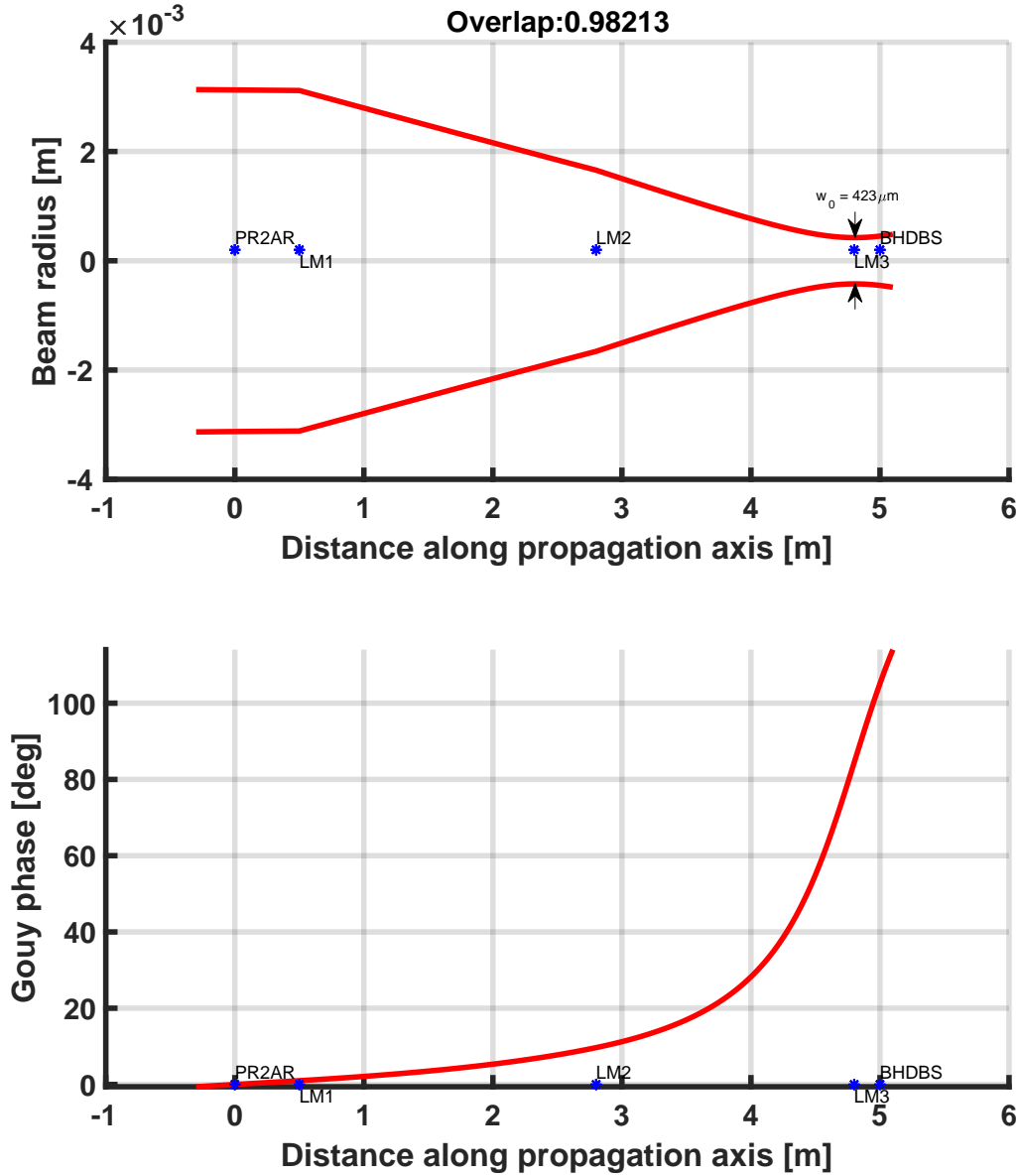


Figure 6: Mode-matching telescope for the LO beam (from PR2 AR surface to the OMC input coupler). The total distance is assumed to be 5 m. We use the seed beam coming from the PRM side which is converging (instead of the diverging beam from the PR3 side).

Table 2: Parameters of the telescopes. We use z , RoC, α , w , and η to respectively represent the coordinate, radius of curvature, angle of incidence, spot size, and gouy phase. For the AS (LO) path, the $z = 0$ is measured at the SRM AR (PR2 AR).

	Component	z [m]	RoC $\cos \alpha$ [m]	w [mm]	η [deg]
AS path	OM1	0.3	7.895	3.13	0.60
	OM2	2.024	-150	1.83	6.43
	OM3	4.3	Inf	0.461	72.8
LO path	LM1	0.5	10.0	3.12	1.00
	LM2	2.8	21.429	1.66	9.67
	LM3	4.8	Inf	0.424	84.4

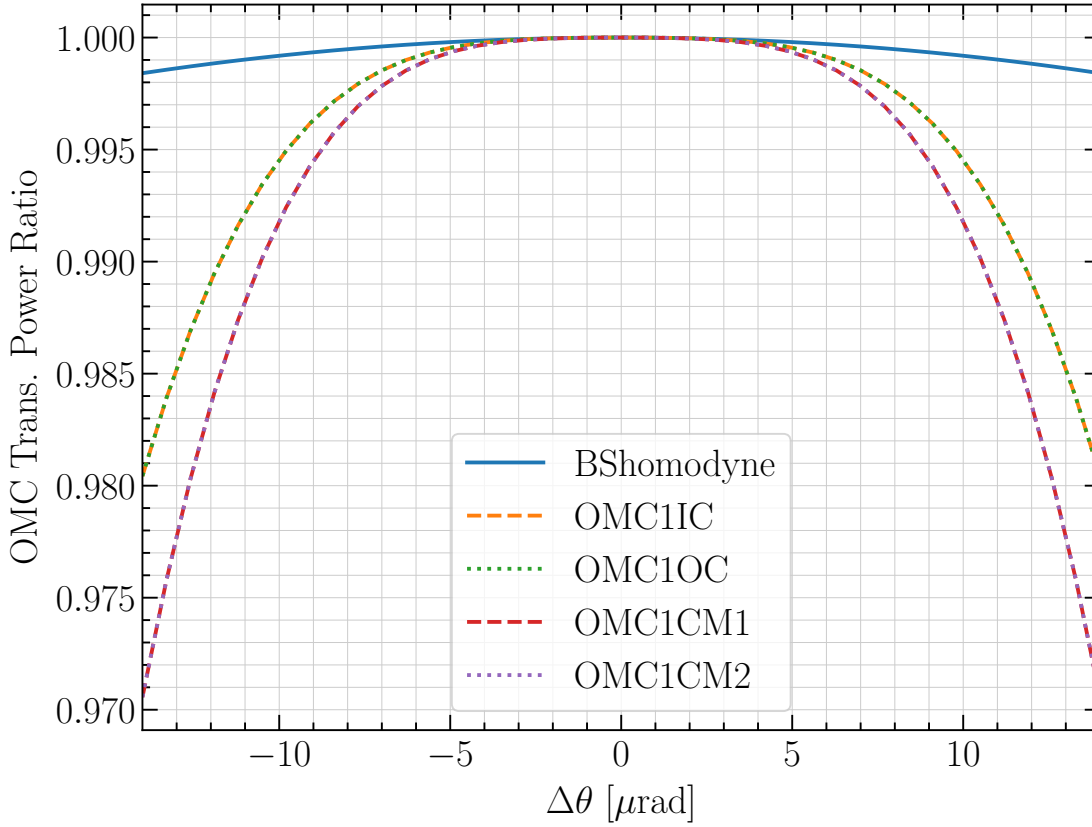


Figure 7: Fractional power build-up as a function of OMC mirrors' misalignment.

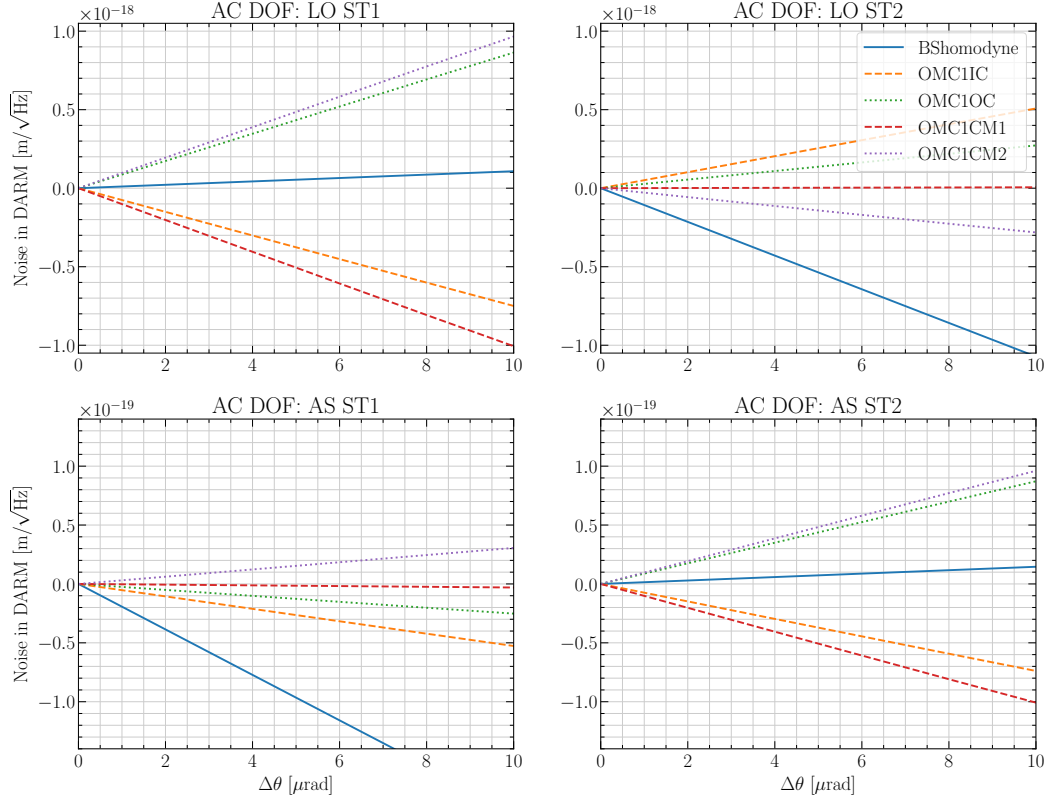


Figure 8: The angle-to-length projection due to BHD board's internal misalignment. In each panel, we have assumed one of the LO/AS steering mirrors having a flat noise spectrum of $1 \text{ nrad}/\sqrt{\text{Hz}}$. The steering mirrors 1 and 2 are separated by 90 degree of goup phase yet we fix the spot size on them to be the same as the one on the homodyne BS (0.5 mm).

The DC internal misalignment can couple with the AC angular noise from the LO/AS steering mirrors to create a noise in DARM. Note that even the AC angular motion of the AS path matters because the AS beam contains some residual 00 field due to the imbalance of the two ITMs' losses. Assuming a flat noise spectrum of $1 \text{ nrad}/\sqrt{\text{Hz}}$, the noise projection onto DARM is shown in Figure 8.

3.3.2 Aligning the LO/AS beams to the OMC board

One possible way of achieving the homodyne alignment is to first align the LO beam to the BHD board, and then align the AS beam to the LO beam. In this Section we consider several possible error signals.

To convert the shot-noise-limited sensitivity in $\text{rad}/\sqrt{\text{Hz}}$ into a control bandwidth requirement, we assume a fixed the control-loop shape shown in Figure 9.

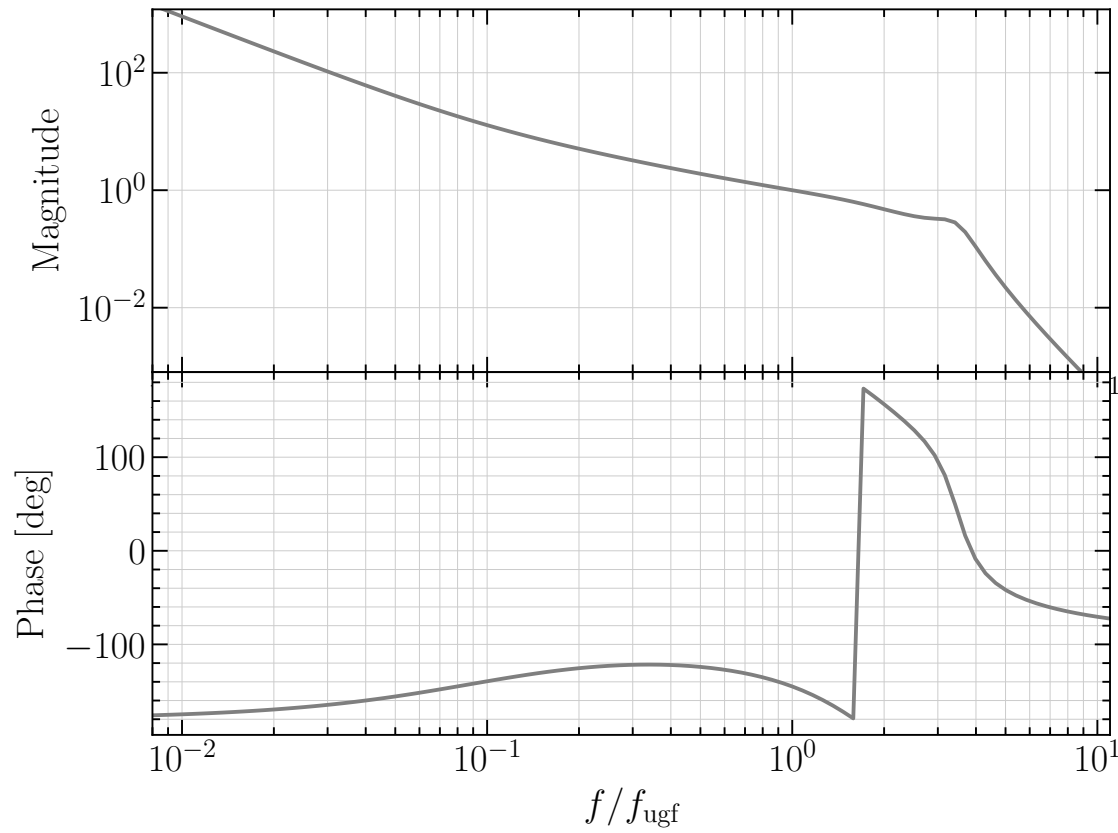


Figure 9: The loop shape we assume for the angular control. Here we allow the unity gain frequency f_{ugf} to be a free parameter while fixing the spectral shape when the frequency is measured in f_{ugf} .

Aligning the LO to the BHD board To align the LO beam, we can dither the LO steering mirrors and demodulate the power on each OMC's transmission as the error signal. Using this signal, we can achieve a sensitivity of

$$\Delta\theta_{\text{LO}} = 2 \times 10^{-10} \left(\frac{\theta_{\text{dith}}}{1 \mu\text{rad}} \right) \text{ rad}/\sqrt{\text{Hz}}. \quad (1)$$

Alternatively, we can use a DC QPD which picks up some light between the BHD BS and the OMC. Strictly speaking this is not an interferometric signal (it responds to both signals due to the misalignment between the LO and the BHD board, and signals due to the alignment to the PD itself). Nonetheless, since it can be rigidly mounted onto the same board as the BHD setup, we can treat the alignment to the PD itself is perfect. This gives a better sensitivity compared to the dithering scheme (assuming picking up $\mathcal{P} = 1\%$ of the light)

$$\Delta\theta_{\text{LO}} = 1 \times 10^{-11} \left(\frac{\mathcal{P}}{1\%} \right)^{-1/2} \text{ rad}/\sqrt{\text{Hz}}. \quad (2)$$

Aligning the AS to the LO/BHD board The alignment of the AS beam is challenging as there is no bright carrier field. One possibility is to assume that the f2 side band is co-aligned with the carrier beam in the AS path and then align it to the carrier (or f1) field from the LO/path. We can then readout the signal from RF WFS on the reflection of OMCs. Since the carrier is nearly critically coupled to the OMC, on the reflection side the (f2-f1) signal (beatnote between f1 and f2) is comparable in sensitivity to the f2 signal (carrier-f2 beatnote). However, this would require RF WFS which is expensive.

Alternatively, one may try to derive the signal based on some dithering schemes. One possibility is to dither ETMs differentially in angle, then if the AS path is misaligned with respect to the DARM cavity's axis, there will be power fluctuations at the dithering frequency in the DC PDs after the OMCs. One can then readout this signal from the SUM or DIFF channels. However, this signal is degenerate with the common ETM alignment. As shown in Figure 10, a few nrad of residual common ETM misalignment can produce an error signal corresponding to tens of microradians of the OMs' (i.e. steering mirrors in the AS path) misalignment.

The way around it is to do double dithering again. We dither DARM in length and then also dither the OMs in angle. We can then look at the DARM response at the beat-note between the two AF ditherings. This is illustrated in Figure 11. As FINESSE does not support two AF ditherings, in the plot we only dither DARM in length and vary the OM alignments in DC to see the second-order reduction of DARM response. Also shown is the DARM response as a function of differential ETM alignment (top axis; the results for common ETM alignment is very similar). A few nrad of ETM alignment offset is a small in reducing DARM response compared to a few microradians of OM misalignment.

Once the DC point is set, we can then use the DC QPDs to stabilize the AC alignment fluctuations of the AS path.

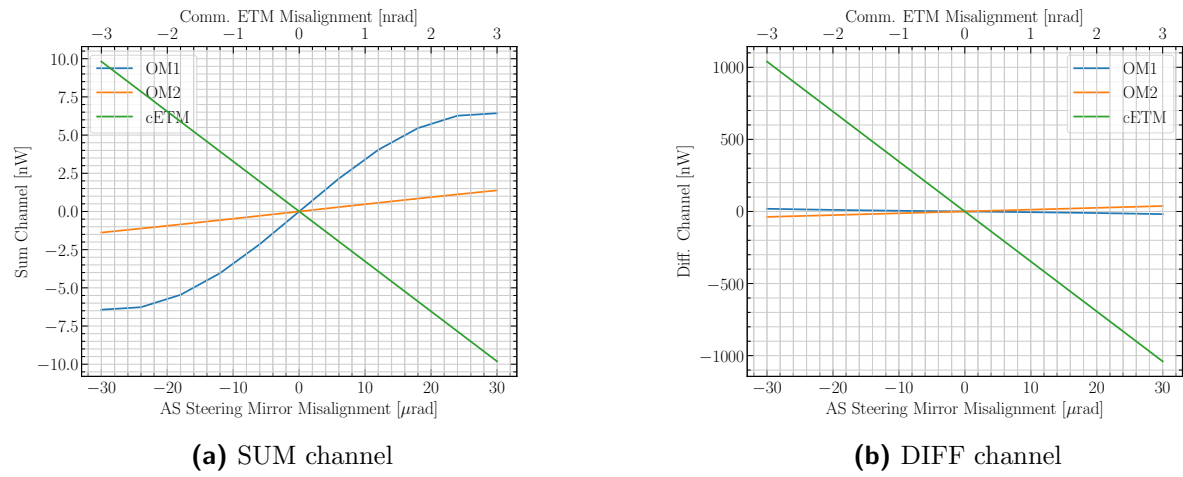


Figure 10: Dithering differential ETMs and demodulate the power from DC PDs on the OMC transmission. The error signal is largely degenerate with common ETM alignment and is thus likely to be biased due to the residual ETM motion.

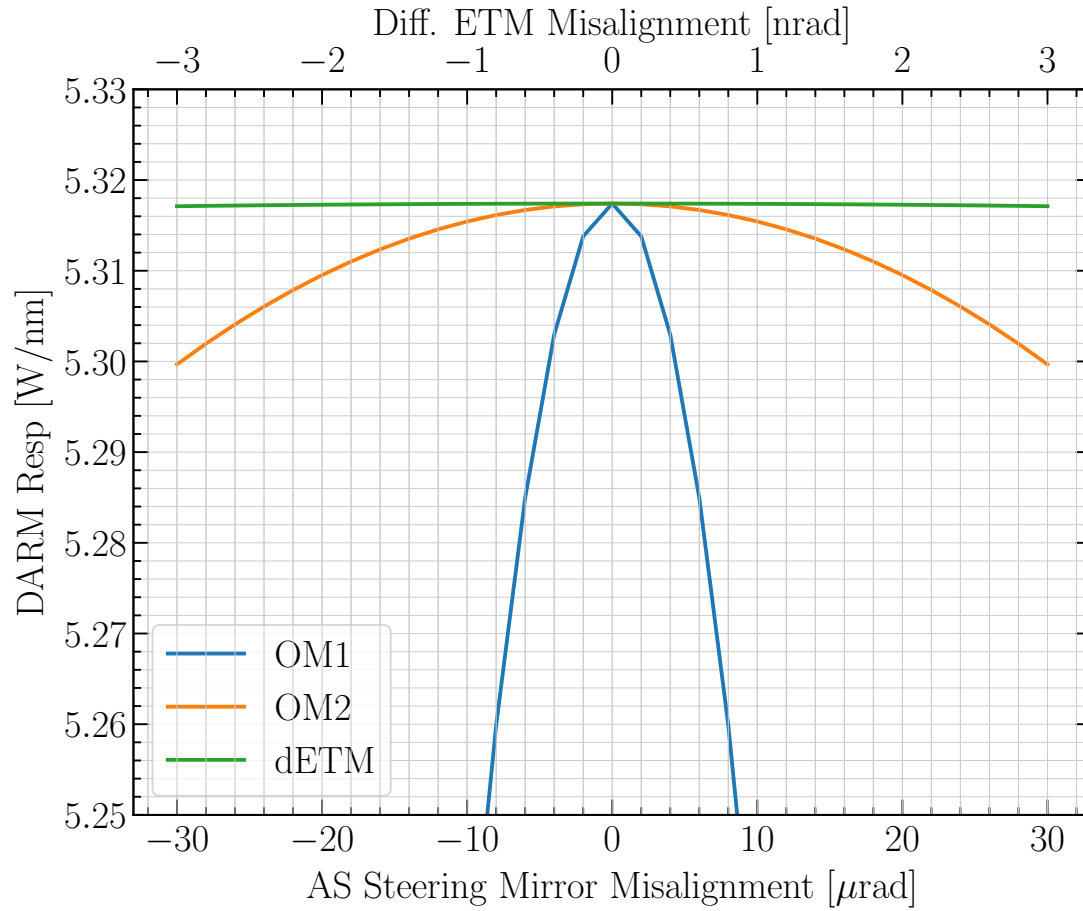


Figure 11: DARM response as a function of the OM's misalignment (bottom axis) or the ETM misalignment (top axis). The OM's sees less contamination from the ETMs as compared to Figure 10.

4 Performance requirements

The **BHD** readout system is being considered as the nominal configuration for the A+ detectors. The A+ interferometers are expected to be operated in the **Resonant Sideband Extraction (RSE)** configuration, and hence we assume the homodyne angle to be $\zeta = 0^\circ$. For all references to the homodyne angle, we follow the convention used in [1] (i.e., $\zeta = 0^\circ$ corresponds to the phase quadrature). The realized **BHD** system should be able to achieve shot noise-limited readout sensitivity in the band 10 Hz – 5 kHz, with all noises associated with the **BHD** system a safety factor of 10 below the next highest noise source in the **Differential Arm Motion (DARM)** noise budget in the target frequency band.

5 Local oscillator requirements

While **BHD** has been proven to achieve shot-noise-limited sensitivity in tabletop experiments, the main challenge to its implementation in large-scale interferometers is the presence of significant contrast defect power (typically several mW) at the anti-symmetric port. Defect light arises from differential losses along the two arm paths and from imperfect spatial mode-overlap at the beamsplitter (see Appendix A.1 for a detailed discussion).

We assume that the **OMC** cavities are well matched to the common arm mode, so that the higher-order spatial modes will be sufficiently attenuated (hence are neglected in this analysis). However, differential losses introduce an amplitude imbalance between the fields of the two arms, resulting in residual power in the TEM00 mode which is transmitted to the photodetectors. As shown in [4], residual power in the signal path amplifies the noise variance of the **LO** field by a proportionate factor, leading to stringent requirements on **LO** stability.

This section presents the required amplitude and phase stability of the **LO**, as determined from optical modeling of the proposed topology (see Figure 1). The analysis relies on several assumptions:

1. The **LO** power is assumed to be 100 mW. If the **LO** beam is picked off at PR2, as proposed in Figure 1, achieving this power will require the existing mirror to be replaced with a more transmissive optic.
2. **RF** sidebands and higher-order modes are neglected, as these fields will be strongly attenuated by the **OMCs**.
3. The **LO** and interferometer modes are assumed to be perfectly matched to each other and to the TEM00 mode of the **OMCs** (i.e., mode-mismatch losses are neglected). Mode-mismatch losses are considered separately in Section 8.

The residual power in TEM00 (contrast defect) is expected to be ~ 1 mW. However, because this value is not precisely known, we will treat it as an unknown variable.

5.1 Relative intensity noise

Figure 12 shows the **LO RIN** requirement as a function of homodyne angle and contrast defect power. The blue marker indicates the expected nominal operating point. As the figure shows, the coupling of **LO** intensity fluctuations vanishes to first order approaching

the phase quadrature. Within 0.1° of detuning from phase quadrature readout, the intensity stabilization requirement is $> 10^{-6}/\sqrt{\text{Hz}}$.

5.2 Phase noise

Figure 13 shows the overall LO phase noise requirement as a function of homodyne angle and contrast defect power. The blue marker indicates the expected nominal operating point. Allowing for a safety factor of 10, nominal readout requires LO phase stabilization to $1.0 \times 10^{-9} \text{ rad}/\sqrt{\text{Hz}}$.

Phase fluctuations of the LO field arise from both (1) optical fluctuations of the laser frequency or phase and (2) physical displacements of the relay path length. There are several sources of length noise in the relay path:

1. Seismic noise
2. Length controls noise
3. Actuator noise of the relay optics

In the following sections, we derive individual requirements on each source of path length noise.

5.2.1 Seismic isolation of relay optics

From the requirement on total LO phase noise obtained in Section 5.2, requirements on the seismic isolation of the suspended relay optics can be derived. The locations of the LO relay optics are shown in Figure 1 (denoted LM1-5). The total phase noise requirement is projected to units of longitudinal displacement *per optic* as

$$\Delta x_{\text{max}} = \frac{\lambda}{4\pi} \frac{\Delta \phi_{\text{max}}}{\sqrt{N}} , \quad (3)$$

where the number of optics $N = 5$ and the additional factor of 2 in the denominator accounts for the imprinting of the phase shift in reflection. Each optic is assumed to couple similarly to the seismic background.

Figure 14 shows the displacement noise requirement for the relay optics, again assuming a safety factor of 10. The blue curve represents the displacement noise requirement for nominal readout ($\zeta = 0^\circ$). Around the expected operating point, indicated by the yellow line, the displacement noise requirement (per optic) is $3.7 \times 10^{-17} \text{ m}/\sqrt{\text{Hz}}$.

The above requirement represents the maximum displacement noise, at any given frequency, to achieve shot noise limited readout sensitivity. However, the vibration isolation required of the suspension system is strongly dependent on frequency, due to the intrinsic variation of the seismic noise spectrum. The required vibration isolation factor is given by the ratio

$$I(f) = \frac{\Delta x_{\text{max}}}{\Delta x_{\text{stack}}(f)} , \quad (4)$$

where Δx_{stack} is the longitudinal vibrational noise coupled through the seismic isolation stacks supporting the chamber tables. We estimate the displacement noise of the tables as

$$\Delta x_{\text{stack}}(f) = T_{xx}(f) \Delta x_{\text{seis}}(f) + T_{xz}(f) \Delta z_{\text{seis}}(f) , \quad (5)$$

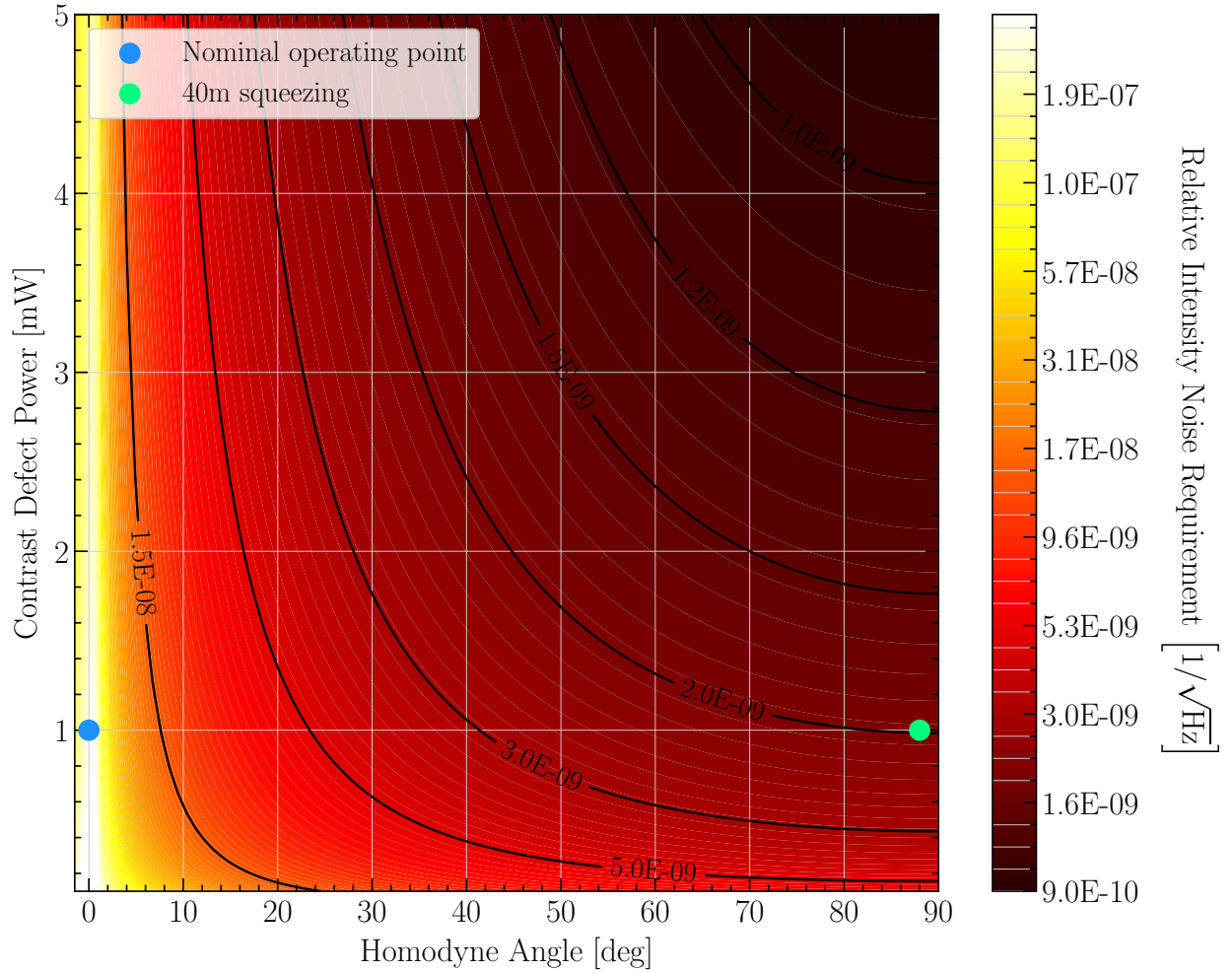


Figure 12: LO RIN requirement as a function of homodyne angle and contrast defect power. The blue marker indicates the expected nominal operating point. The coupling of LO intensity fluctuations vanishes to first order approaching the phase quadrature. Within 0.1° of detuning from phase quadrature readout, the intensity stabilization requirement is $> 10^{-6}/\sqrt{\text{Hz}}$. Near the green marker, representing the 40m ponderomotive squeezing experiment (see Appendix C), intensity stabilization to $2.0 \times 10^{-9}/\sqrt{\text{Hz}}$ is required.

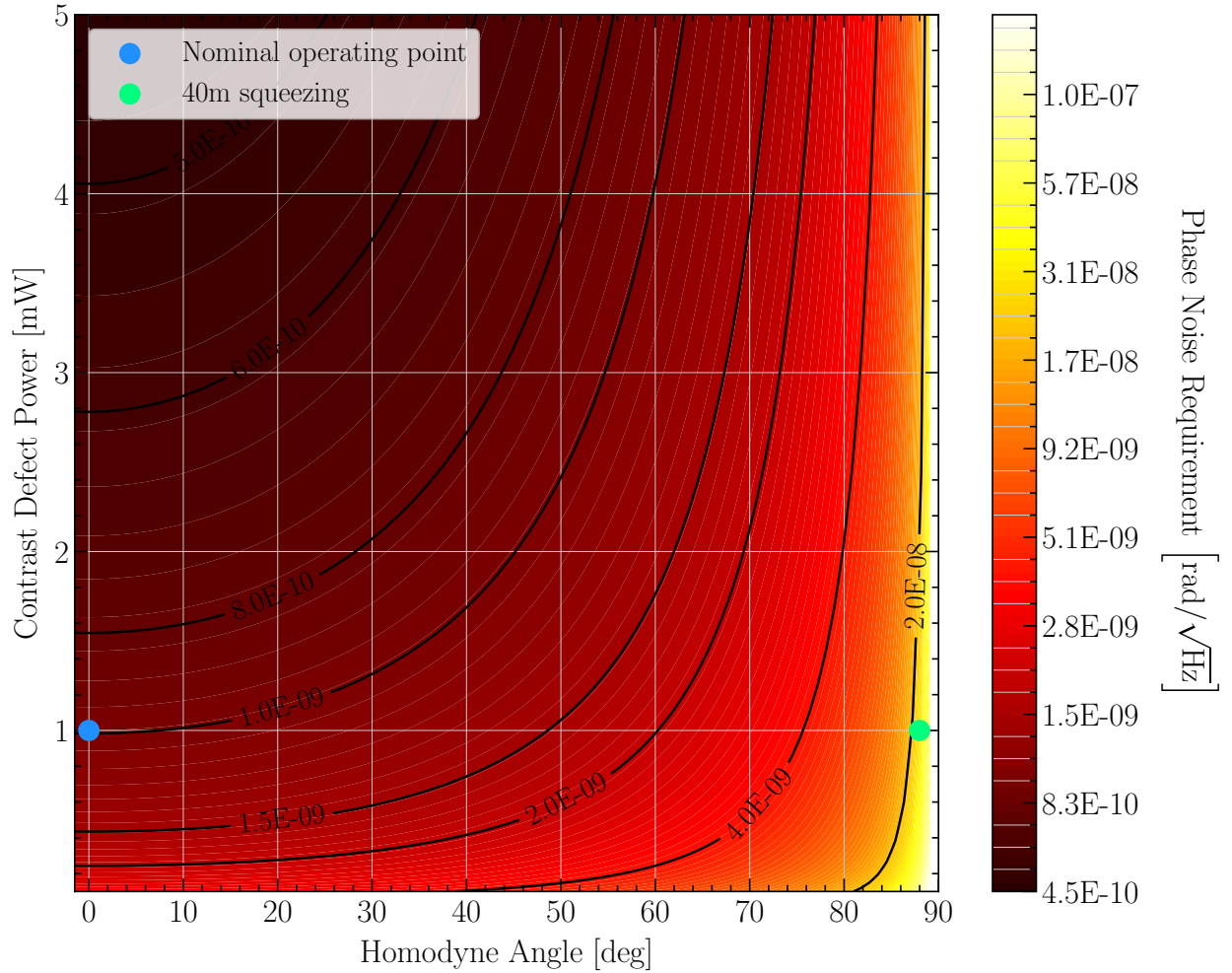


Figure 13: LO phase noise requirement as a function of homodyne angle and contrast defect power. The blue marker indicates the expected nominal operating point. Allowing for a safety factor of 10, nominal readout requires LO phase stabilization to $1.0 \times 10^{-9} \text{ rad}/\sqrt{\text{Hz}}$. Near the green marker, representing the 40m ponderomotive squeezing experiment (see Appendix C), phase stabilization to $2.8 \times 10^{-8} \text{ rad}/\sqrt{\text{Hz}}$ is required.

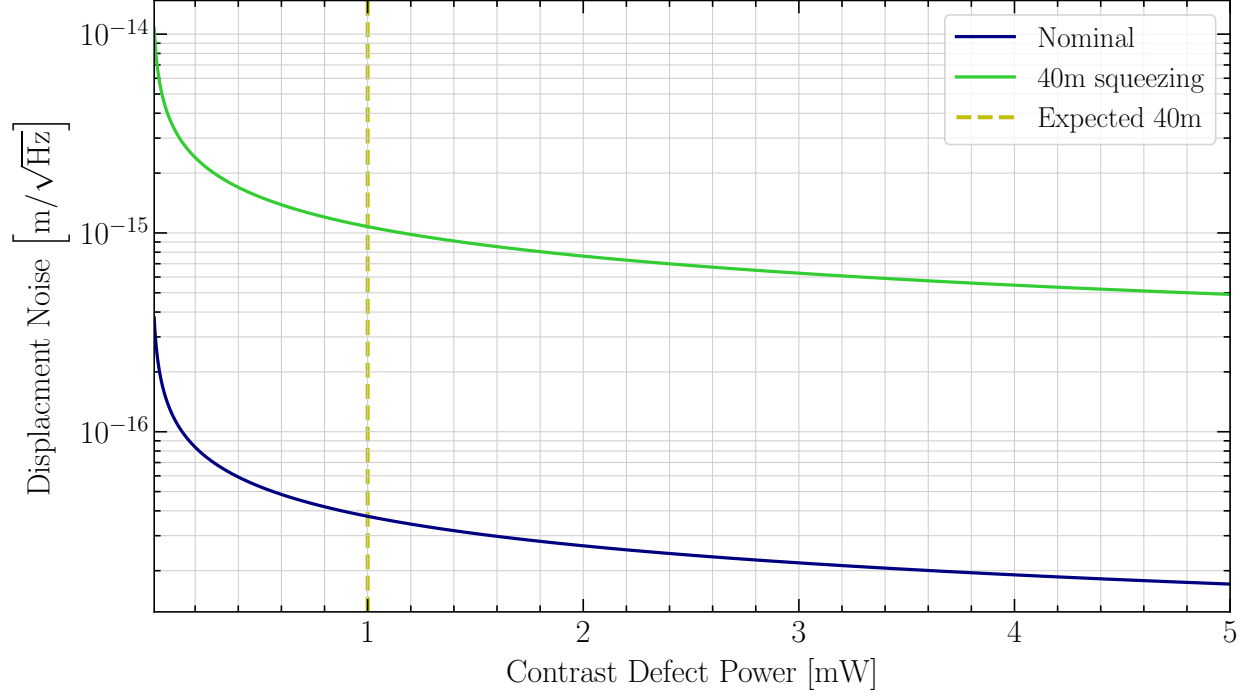


Figure 14: Displacement noise requirement per relay suspension, assuming 5 optics in the LO path. The total phase noise requirements shown in Figure 13 are projected to longitudinal displacement of the relay mirrors, as described in Section 5.2.1. The blue curve represents the displacement noise requirement for nominal readout ($\zeta = 0^\circ$). Around the expected operating point, indicated by the yellow line, the displacement requirement (per optic) is $3.7 \times 10^{-17} \text{ m}/\sqrt{\text{Hz}}$. For the 40m ponderomotive squeezing experiment (see Appendix C), represented by the green curve, the requirement is $1.1 \times 10^{-15} \text{ m}/\sqrt{\text{Hz}}$.

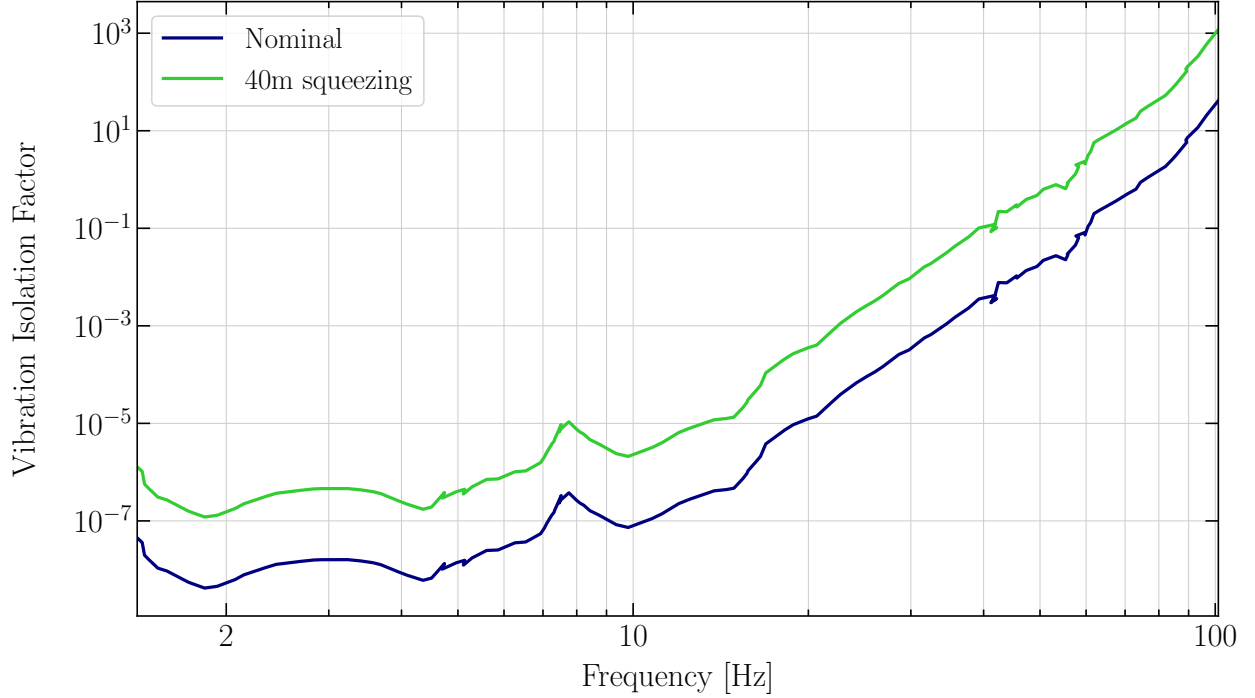


Figure 15: Required vibration isolation factor of the LO relay optic suspensions. This requirement is estimated from the longitudinal displacement requirement shown in Figure 14 for 1 mW of contrast defect power and from motion-transfer measurements of the seismic isolation stacks from Giaime et al. [5].

where T_{xx} and T_{xz} are the couplings of horizontal and vertical seismic motion, Δx_{seis} and Δz_{seis} , respectively, to horizontal motion of the chamber tables. These couplings are measured by Giaime et al. [5] for the stack design installed in the 40m interferometer. For the directional seismic noise backgrounds, Δx_{seis} and Δz_{seis} , we assume the isotropic noise model from Giaime et al. [5] for a “typical” site environment. Figure 15 shows the required vibration isolation factor for nominal readout (blue curve).

5.2.2 Actuator noise

In addition to seismic noise, electronics noise of the relay optic actuators also produces displacement noise. For each optic, we estimate its actuator noise as the sum of electronics noise contributions from the Digital to Analog Converter (DAC) and coil drivers, propagated to the resulting physical displacement. The electronics noises are estimated for the equipment currently installed in the 40m.

We estimate the DAC voltage noise using the empirical model from elog #13003,

$$\Delta V_{\text{DAC}}(f) = 700 \times \sqrt{1 + \frac{100 \text{ Hz}}{f}} \times \left(10^{-9} \text{ V}/\sqrt{\text{Hz}} \right). \quad (6)$$

This noise is then propagated through a dewhitening filter between the DAC and coil driver. We model the dewhitening filter as a fourth-order type II Chebyshev low-pass filter, with a

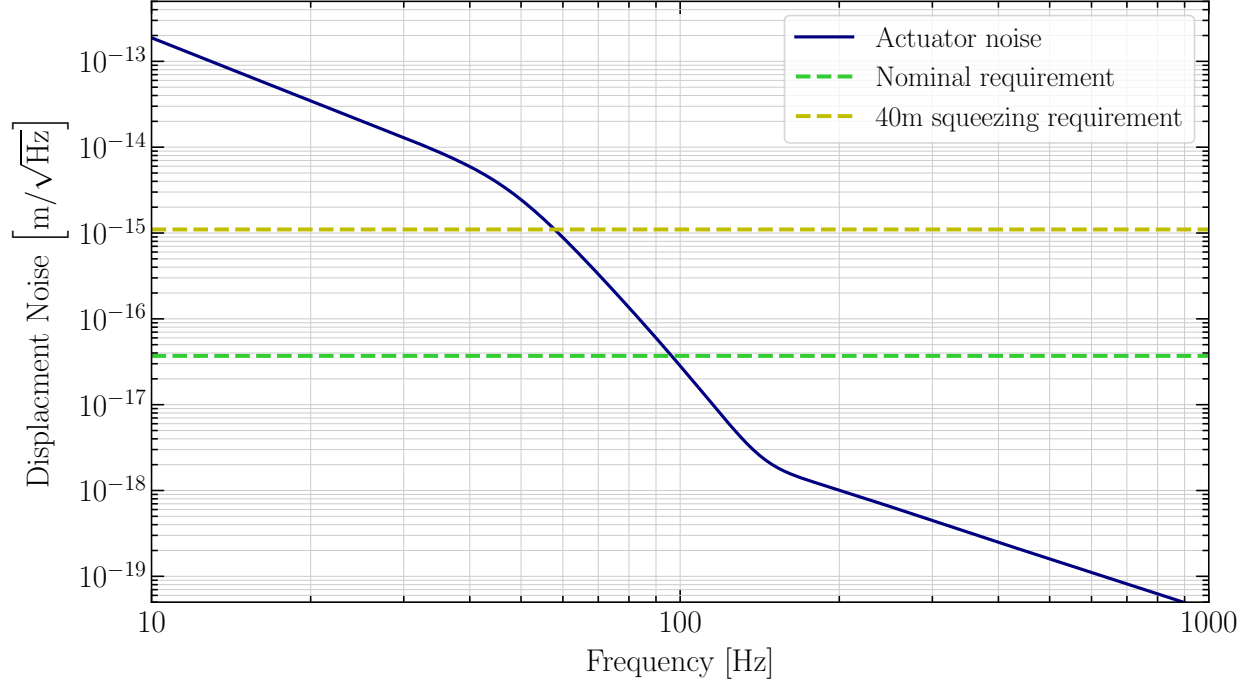


Figure 16: Actuator noise per suspended relay optic. Shown is the sum of contributions from DAC noise and coil driver noise, propagated to units of longitudinal displacement. The dashed lines indicate the overall displacement noise requirement per optic (see Figure 14), assuming 1 mW of contrast defect power and a safety factor of 10. With the current 40m electronics, the BHD readout sensitivity will be limited by actuator noise below 70 Hz (30 Hz for the 40m ponderomotive squeezing case).

passband of 30 Hz and a stopband above 300 Hz. The coil driver voltage noise, ΔV_{CD} , is calculated from a linear model of the coil driver circuit.

The quadrature sum of the two voltage noises, ΔV_{act} , is propagated to mirror displacement noise as

$$\Delta x_{act} = \Delta V_{act} \times \left(\frac{1}{400 \, \Omega} \right) \times \left(\sqrt{4} \times 0.016 \, \text{N/A} \right) \times \left(\frac{1}{\pi^2 f^2} \right), \quad (7)$$

where the calibration terms, from left to right, represent the progressive propagation to current noise, to force noise, and finally to displacement noise. In Equation (7), $400 \, \Omega$ is the series resistance of the coil driver, the $\sqrt{4}$ accounts for four coil drivers per optic, and the $1/f^2$ term is the pendulum transfer function above its resonant frequency (~ 1 Hz).

Figure 16 shows the resulting actuator noise per relay optic. For reference, the dashed green line denotes the overall displacement noise requirement per optic (see Figure 14), assuming 1 mW of contrast defect power and a safety factor of 10. This indicates that, with the current 40m electronics, the BHD readout sensitivity will be limited by actuator noise below 70 Hz.

6 Output mode cleaner requirements

The **OMC** that we use is based on the aLIGO design: a bowtie configuration with two flat mirrors and two curved mirrors, a finesse of ~ 400 , and an angle of incidence of $\sim 4^\circ$. For more details on the **OMC** design considerations, see Appendix B.

6.1 Functions of the OMC cavity

The **OMC** is a cavity that is installed between the **Interferometer (IFO)** output and the readout DCPDs. The functions of the **OMC** are:

1. To filter out the RF sideband frequency content from the IFO AS and LO fields.
2. To filter out higher-order HG modes of the carrier field, that may be generated due to mismatched optical cavities and/or misalignments.
3. Transmit the DARM signal to the DCPDs with as little optical loss as possible.

6.1.1 Spectrum of input mode content

The filtering performance of the **OMC** is determined by the cavity finesse. However, the actual amount of junk light that makes it onto the **OMC** DCPDs is dependent on the amount incident as well.

For the aLIGO **OMC**, the filtering requirement is principally on the AS beam from the IFO. The recycling cavity lengths are chosen in such a way that the f_2 sideband is critically coupled to the dark port, while the f_1 sideband mostly remains in the symmetric side (though the leakage to the dark port isn't zero). Consequently, the following power law model was assumed for the power fraction in various carrier HOMs:

$$P_{f_0}(n) [\text{W/W}] = \begin{cases} 0 & n = 0, \\ 7 \times 10^{-5} & n = 1, \\ 1.8 \times 10^{-(3+\frac{n}{4.8})} & n \geq 2. \end{cases} \quad (8)$$

For the f_2 sideband, the following model was assumed for transmission from the PRC to the SRC (the SRC cavity's resonance structure is neglected):

$$T_{f_2}(n) = \begin{cases} 1 & n = 0, \\ 1.7 \times 10^{-1} & n = 1, \\ 7 \times 10^{-(1+\frac{n}{2})} & n \geq 2. \end{cases} \quad (9)$$

Finally, for the f_1 sideband, it was assumed that $T_{f_1} = T_{f_2}/1000$. This model neglects (i) mode-healing / mode-harming effects of the SRC, and (ii) the actual transmissivity of the f_1 sideband with the SRC included. For the BHD setup, the OMC also needs to clean up the LO field, which is in fact picked off from the symmetric side of the interferometer. At first glance, this may suggest that the LO field will have strong f_1 content because the PRC is designed to be resonant for this field. However, assuming that the LO field is picked off from the transmission of a **High-Reflectivity (HR)** mirror (as is proposed), we estimate that the

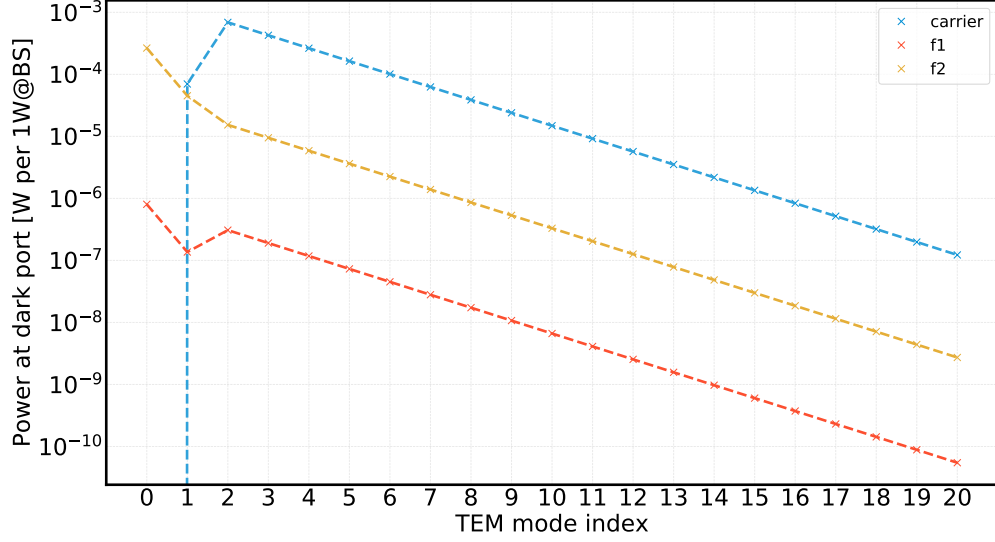


Figure 17: Assumed model spectrum of power in HOMs.

power of the f_1 content in the LO beam will be *approx* $1000 \times$ lower than the power of the f_2 field in the antisymmetric port beam, and hence, we did not change the spectral model assumed. The model assumed is shown in Figure 17.

6.1.2 Cavity round-trip length

The cavity round-trip length should be chosen such that the RF sideband TEM_{00} modes are not resonant in the [OMC](#) when the carrier is resonant. For the 40m, the RF sideband frequencies are (i) $f_1 = 11.066209$ MHz and (ii) $f_2 = 5 \times f_1$.

To convert frequency offset from the carrier to phase offset, we use the relation

$$\phi_{\text{RT}}^{\text{SB}} = \frac{2\pi f^{\text{SB}} L_{\text{RT}}}{c} \quad (10)$$

The [OMC](#) power transmissivity is given by

$$T_{\text{OMC}} = \left| \frac{t_{\text{F}}^2}{1 - r_{\text{C}}^2 r_{\text{F}}^2 e^{-i\phi}} \right|^2, \quad (11)$$

so we can just examine what this looks like for the TEM_{00} mode of the RF sidebands as a function of the round-trip length of the cavity.

6.1.3 Higher order modes

Equation 10 can be generalized for higher order HG modes by realizing that the mn – th HOM experience an additional phase shift of $(m + n) \times \zeta$ relative to the TEM_{00} mode, with ζ being the round-trip cavity Gouy phase which can be calculated from an ABCD matrix. This number is always additive, whereas the phase offset from the carrier due to the field being an RF sideband is a signed number, depending on whether we are considering the

upper or lower sideband. So the ϕ that enters the cavity transmission equation may be broken up into the following components:

$$\phi_{\text{RT}}^{mn}(f) = \phi_{\text{RT}}^{00}(0) + \frac{2\pi f_{\text{RF}}^{\text{SB}} L_{\text{RT}}}{c} + (m+n)\zeta. \quad (12)$$

Plugging this into Eq. 11 for T_{OMC} , we get the power transmissivity of the OMC cavity.

The outcome of the modeling is shown in Figure 18, with the suggested operating point indicated by dashed green lines. We chose to preserve the curvature specification for the mirrors to be identical to the aLIGO OMC [6], 2.575 m, and scanned the cavity length to account for the different sideband frequencies at the 40m. The cavity round-trip length is chosen to be 0.875 m. For comparison, the aLIGO OMC design parameters are indicated by dashed cyan lines. The one-dimensional slices along the dashed green lines are shown in Figure 18b and Figure 18c, with the vertical pink lines indicating the suggested design parameters.

6.2 Finesse

(Shruti is working on the OMC finesse requirement.)

6.2.1 Required balancing between OMCs

(Shruti is also working on the required balancing.)

6.3 Length noise

When the OMC is on resonance, fluctuations in its length do not cause intensity noise to first order. However, the locking precision of the OMC is limited by its length sensing noise, which gives rise to a typical detuning Δl_{RMS} . Such detuning linearly couples noise from small fluctuations δl , such as Brownian motion, to the output of the OMC. Quantitatively, the intensity noise at the OMC output is related to the OMC length fluctuations through the transmission function of the OMC,

$$\frac{\delta P}{P} = 1 - \left[1 + \left(\frac{2\mathcal{F}}{\pi} \right)^2 \sin^2 \left(2\pi \frac{\Delta l_{\text{RMS}} + \delta l}{\lambda} \right) \right]^{-1} \approx 32 \mathcal{F}^2 \frac{\Delta l_{\text{RMS}} \delta l}{\lambda^2}, \quad (13)$$

where \mathcal{F} is the finesse of the OMC and λ is the wavelength of light.

Figure 19a shows the detection noise induced by the Brownian motion of the Piezoelectric Transducer (PZT) mirror actuators (as described in the OMC thermal noise section below) relative to shot noise, as a function of the Root-Mean-Square (RMS) length detuning and frequency. The length detuning is treated as quasi-static, while the thermal fluctuations are dynamic and much smaller in magnitude. By requiring the total noise coupling be an order of magnitude less than shot noise, we obtain the required OMC length stability shown in Figure 19b. The solid lines show the analytical calculation given by Equation (13). At 100 Hz, the OMC length noise requirement is $1.3 \times 10^{-12} \text{ m}/\sqrt{\text{Hz}}$.

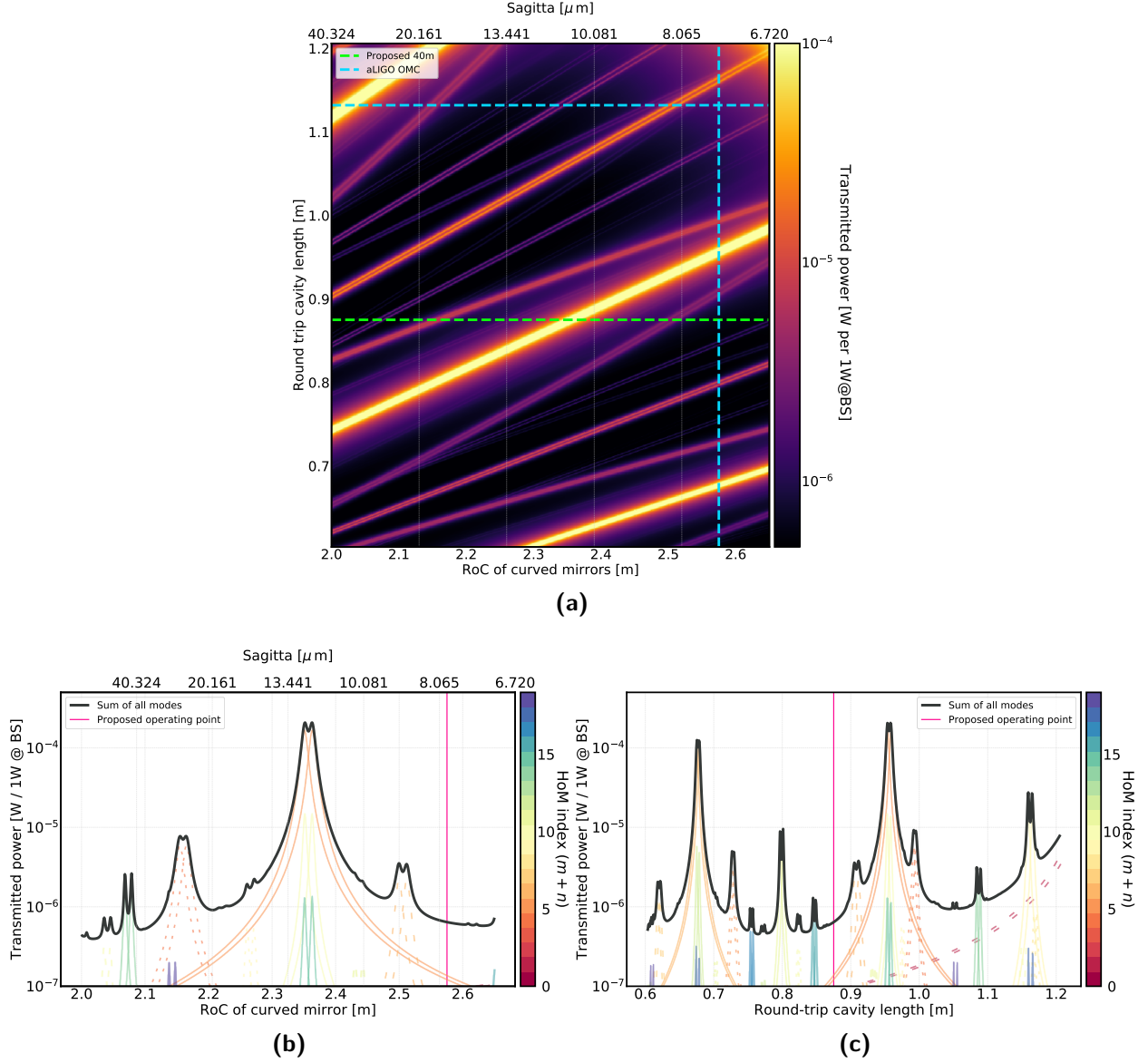


Figure 18: OMC design modeling results. (a) Heatmap of the OMC transmission as a function of the parameters L_1 and ROC. For the 40m RF sideband frequencies, the appropriate choice of L_1 and ROC are 0.875 m and 2.575 m respectively, with $\theta_i = 4.042^\circ$. (b,c) One dimensional slices of the heatmap in (a). The recommended design parameter choice is indicated by a vertical pink line. The various Higher-Order Mode (HOM) resonances are shown by colored lines, with their sum shown in a thick grey line. The different linestyles are used to indicate different sideband frequencies.

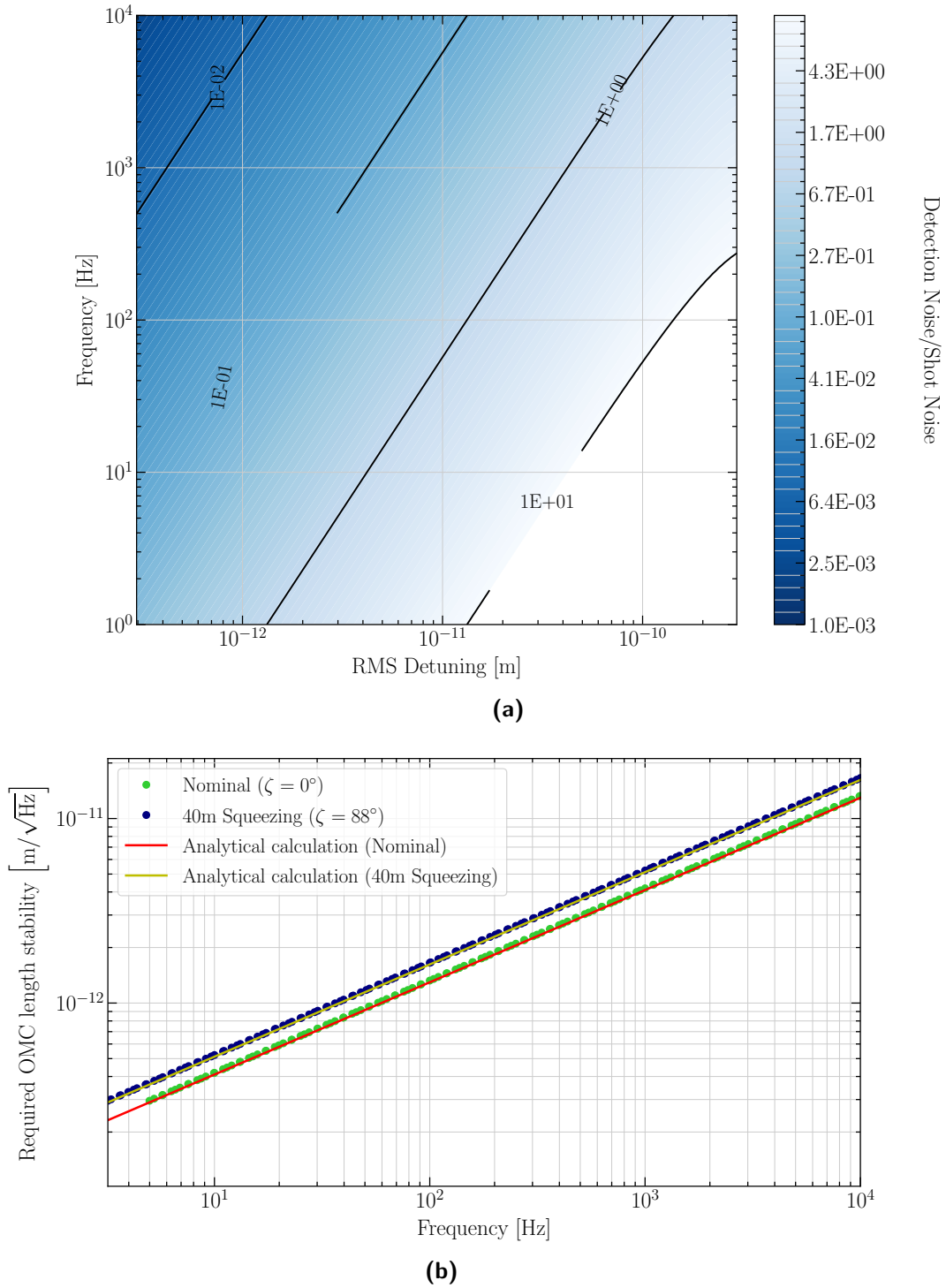


Figure 19: Modeling of OMC length noise induced by Brownian motion of the PZT actuators. (a) Length noise relative to shot noise as a function of RMS length detuning and frequency for the case of nominal readout (phase quadrature detection). (b) Required RMS detuning to achieve a noise coupling 10 times less than shot noise. The solid lines show the analytical calculation given by Equation (13). At 100 Hz, the OMC length noise requirement is $1.3 \times 10^{-12} \text{ m}/\sqrt{\text{Hz}}$ for nominal readout and $1.6 \times 10^{-12} \text{ m}/\sqrt{\text{Hz}}$ for the 40m ponderomotive squeezing case.

6.4 Angular (pointing) noise

Similar to the case of [OMC](#) length noise coupling, mirror angular noise couples to the detection port when the mirror is misaligned. In addition, angular misalignment mixes spatial modes of the laser beam, which is a source of loss.

We model angular noise coupling using Finesse with the following ingredients: First, we include [HOMs](#) in the model. The beam parameters at the input are set to mode match the OMCs. Second, for each mirror under test, we inject angular noise spectrum whose estimation is described in the following section. Finally, we introduce angular displacement to that mirror and measure the resulting output noise relative to shot noise. We simulate angular noise for steering mirrors before and after the homodyne beamsplitter at various homodyne detection angles. We also consider the angular noise coupling of the OMC suspended breadboard and add it to the overall noise budget. The results are multiplied by $\sqrt{2}$ to account for the pitch and yaw degrees of freedom.

6.4.1 Angular noise estimation

For input angular noise we assume a model in which vertical ground displacement noise is coupled to the suspended mirror through a vibration isolation stack installed at the 40m. The vertical motion is coupled to the mirror's angular degrees of freedom through imperfections in the isolation and/or suspension systems. In detail:

- The ground motion is estimated from seismography measurement at the vertex of the 40m interferometer ([40m elog 13850](#)).
- 40m laboratory vibration isolation stack transfer function is obtained from [T1900636](#). Vertical to vertical transfer function was chosen to simulate worse case scenario.
- The mirror's angular degrees of freedom are modeled as a pendulum with resonant frequency of 1Hz.
- Displacement to angle coupling is roughly estimated from optical lever measurement of ITMY in its useful frequency range 0.5-1.5 Hz ([40m elog 13453](#)) to be ~ 10 rad/m.

In total, the input angular noise, shown in [Fig. 20](#), is estimated to be (Ground displacement noise) \times (Isolation stack transfer function) \times (Suspensions transfer function) \times (Displacement to angle coupling).

6.4.2 Simulation result

[Figure 21](#) shows the result of the angular noise modeling. The input RMS noise used was estimated from the angular noise spectrum to be $0.58 \mu\text{rad}$. The figure shows the detection noise as a function of frequency for various steering mirrors and detection phases. The mirrors labeled as "Pre-BS" are positioned on the beam path before the BHD BS and are 4 m away from the OMC input coupler, while the mirrors labeled as "Post-BS" are positioned after the BHD BS and are 1 m away from the OMC input coupler. It can be seen that for most cases the projected noise is 20db below the shot noise level for frequencies greater than 35Hz.

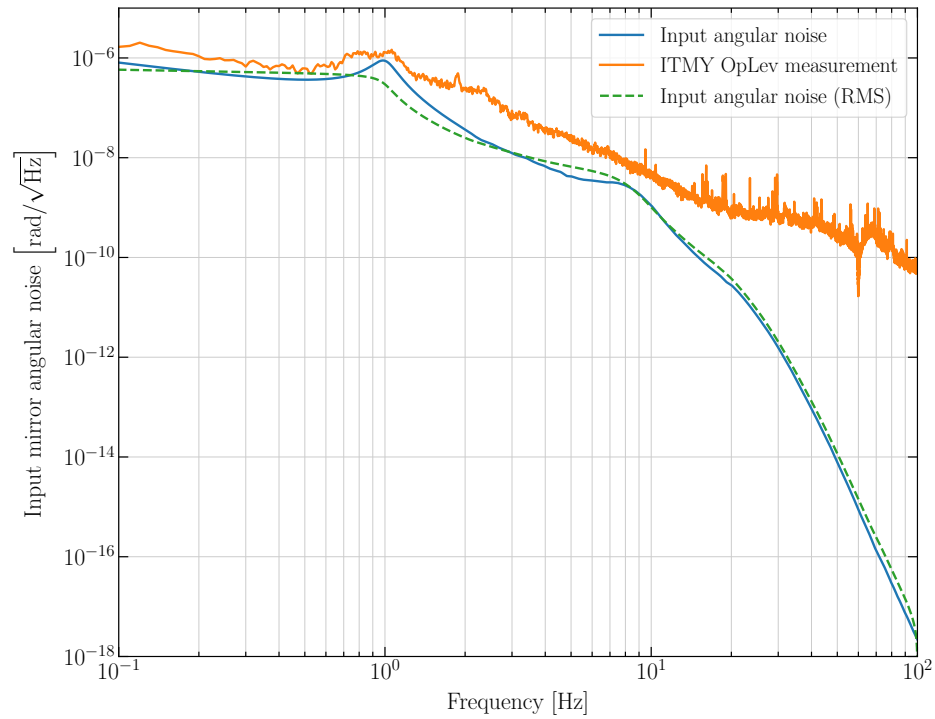


Figure 20: Estimated input mirror angular noise due to ground motion in the vicinity of the mirror. Orange line is the optical lever measurement used for the calibration of the model. Dashed line shows the integrated RMS noise. This spectrum is used as an input to angular noise coupling simulation.

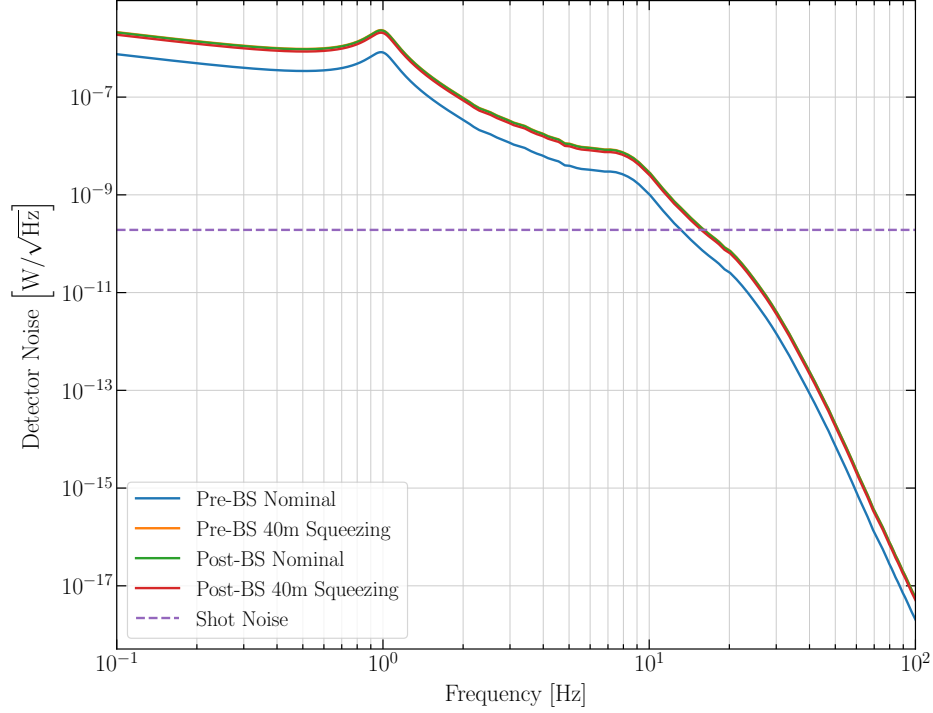


Figure 21: Modeling of steering mirror noise coupling. Detection noise for various steering mirrors and detection quadratures. Dashed line is the Shot noise level.

The case for pre-beamsplitter mirror jittering with phase quadrature readout is special since the detected power is symmetric under displacement of such mirror and therefore is much less noisy than the other cases.

The largest uncertainty in this model is in the value of length to angle coupling constant. However, even if this coupling is two orders of magnitude larger than estimated, the noise at 100Hz would still be 60db below shot noise level.

For the OMC motion when the BHD breadboard is fixed, we lose the vibration isolation at 100 Hz, by a factor of $\sim 10^4$. However, because of the large margin at 100 Hz, the noise caused by this motion is still negligible compared to the shot noise level.

The angular noise of the OMC mirrors was not considered since the expected angular noise due to the brownian motion of the PZTs is ~ 6 orders of magnitude smaller than the angular noise of the suspended mirrors. However, the suspended OMC breadboard is expected to be subject to a vibrational motion similar to that of the steering mirrors. One needs to make sure that mechanical resonances of the breadboard are sufficiently damped.

6.5 OMC thermal noise

One of the fundamental sources of OMC length fluctuations is thermal noise. To estimate the thermal noise, we refer to the calculation of the Brownian motion for the aLIGO OMC. We believe that the result is applicable to the 40m case, since the length fluctuations are dominated by the thermal noise of the PZT actuators.

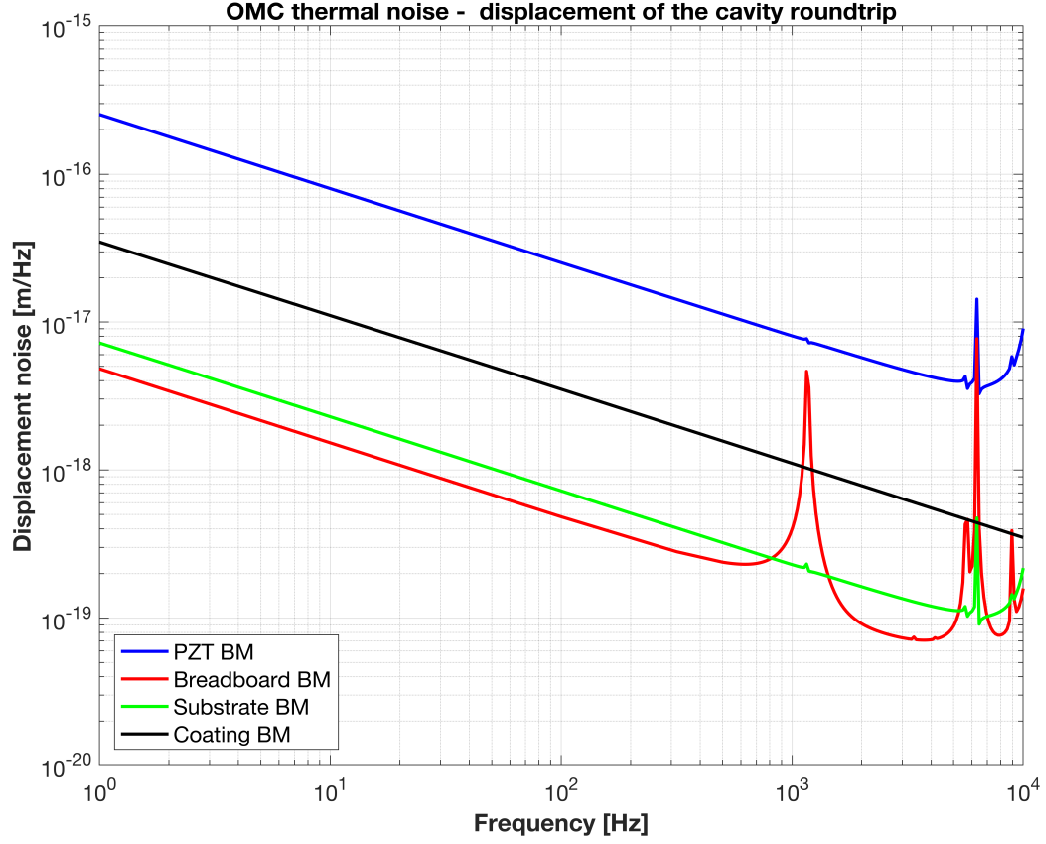


Figure 22: Thermal noise contributions to the **OMC** cavity length fluctuations.

Figure 22 summarizes the result of the calculations described in the following sections. Each thermal noise term is indicated by its amplitude spectral density at 100 Hz and basically has the slope of $f^{-5/2}$. The biggest contribution is the Brownian noise of the **PZT** actuators with an amplitude of $2.5 \times 10^{-17} \text{ m}/\sqrt{\text{Hz}}$. The next biggest contribution is the coating Brownian noise with an amplitude of $3.5 \times 10^{-18} \text{ m}/\sqrt{\text{Hz}}$. The breadboard and prism mirrors that support the **PZTs** and curved mirrors contribute less than $10^{-18} \text{ m}/\sqrt{\text{Hz}}$. The 40m **BHD** plans to use a metal material for the breadboard, at least for the initial attempt. This will make the spacer noise contribution larger by at most a factor of ~ 10 . Therefore, this result suggests that the **PZT** thermal noise will still be the largest contribution.

6.5.1 Coating Brownian motion

We assume a similar coating quality to the one for the aLIGO test masses. Then, we can apply the result of the coating thermal noise calculation by S. Gras [7, Eq. 24] with the spot radius of $500 \mu\text{m}$. The result obtained from this calculation is for a single mirror displacement. Therefore, we multiply it by a factor of $2\sqrt{4}$ to take into account the four mirrors and the roundtrip length.

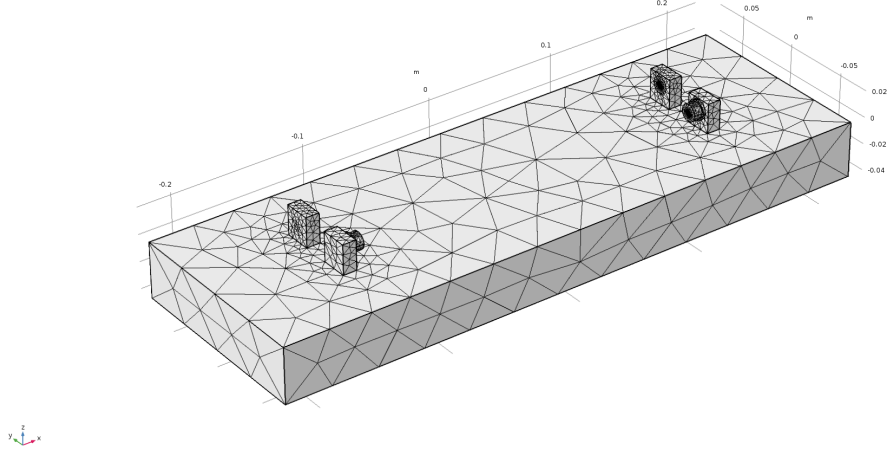


Figure 23: FEA model of the 40m OMC.

6.5.2 Substrate/breadboard/PZT Brownian motion

A Finite Element Analysis (FEA) model, shown in Figure 23, was built in COMSOL for the spacer thermal noise. Y. Levin’s direct approach [8] was used for the calculation.

A pressure force proportional to the light intensity distribution of the laser spots was simultaneously applied to the four mirrors that form the OMC and sinusoidally varied at a frequency f . The stored energy in each part of the body (U_{stored}) was derived by COMSOL, allowing us to estimate the energy loss per cycle as $W_{\text{diss}} = 2\pi f U_{\text{stored}} \phi$, where ϕ is the loss angle of the material. The fluctuation dissipation theorem gives us the amplitude of the thermal fluctuation,

$$x_{\text{BM}}^2 = \frac{2k_{\text{B}}T}{\pi^2 f^2 F_0^2} W_{\text{diss}} , \quad (14)$$

where x_{BM} is the Brownian motion contributed by a particular loss.

The modulation frequency was then swept from $1 - 10^5$ Hz. The applied Gaussian pressure on the four spots was $500 \mu\text{m}$ in e-folding radius. The aLIGO OMC uses Corning 7980 and NCE51F as the materials of the glass parts and the PZTs. In this model, similar materials (Corning 7940 and PZT-5A) were instead used because they are built-in materials in COMSOL. For the loss angle of the fused silica, $\phi(\text{Fused Silica}) = 10^{-7}$ was used. For the piezo, $\phi(\text{PZT}) = 1/80$ was used based on the number from Noliac¹. The result was multiplied by 2 to account for the roundtrip length.

7 Backscattered light requirements

The noise-performance of any scheme used to read out the differential mode of the interferometer can be degraded by scattered light. For the BHD implementation, there are multiple possible pathways through which scattered light can manifest as noise in the readout. Three such examples are shown in Figure 24. For the purposes of this document, we may neglect

¹<http://www.noliac.com/products/materials/nce51f/>

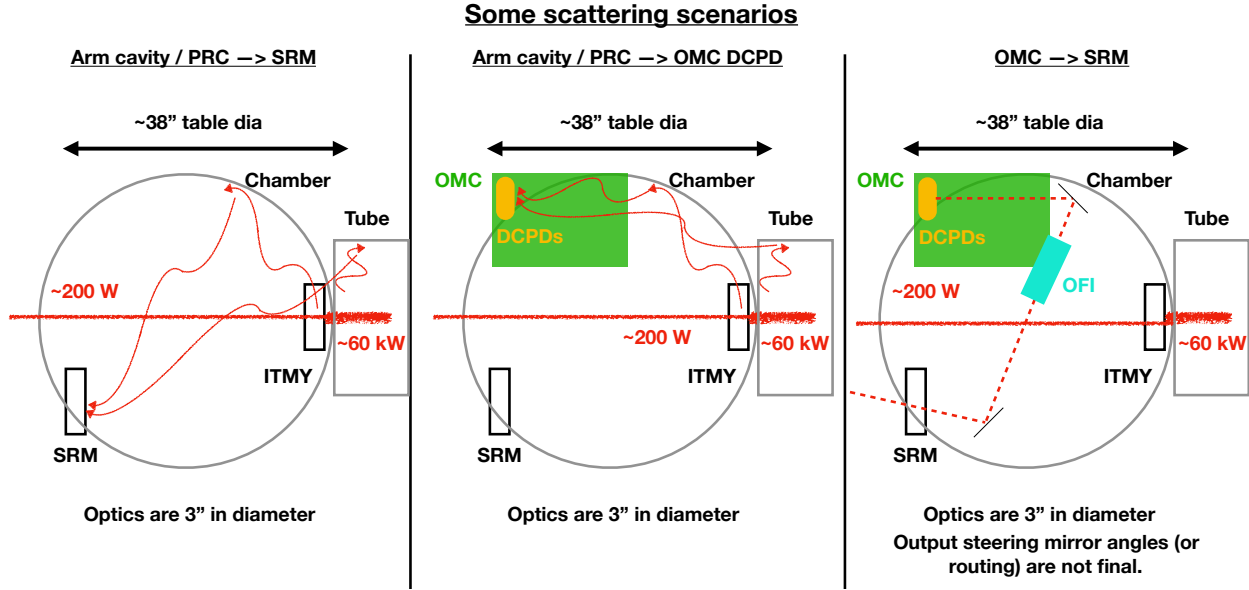


Figure 24: Pathways through which scattered light can degrade the interferometer sensitivity to DARM.

the leftmost panel, as it does not directly set a requirement for the BHD system. The middle panel depicts the pathway where light is directly scattered out of the Fabry-Perot (FP) arm cavities and Power Recycling Cavity (PRC) onto the OMC DCPDs, and is henceforth referred to as direct backscatter. It is discussed in Section 7.1. The rightmost panel depicts a pathway whereby the resonant counter-propagating mode of the OMC contributes a field entering the antisymmetric port of the interferometer, in addition to the (unsqueezed or squeezed) vacuum field. This mechanism will be henceforth referred to as OMC backscatter, and is discussed in Section 7.2.

For the calculations presented in this section, we assume 8 W of optical power incident on the symmetric port of the interferometer, and a Power Recycling Gain (PRG) of approximately 50. The level of unsqueezed vacuum is set by the LO field power, which we assume to be 100 mW, split equally among two OMC cavities.

7.1 Direct backscatter

We assume that the scattered light contribution from the circulating field inside the FP arm cavity dominates any contribution from the circulating field inside the PRC. The fraction of this field that makes it onto the OMC DCPDs is the product of three numbers (referred to as $\epsilon_{\text{scatter}}$):

1. Probability of light scattering out of the TEM00 mode of the arm cavity. This is related to the Bi-directional Reflectance Distribution Function (BRDF) of the Input Test Mass (ITM).
2. BRDF of the scattering surface - in this case, assumed to be the vacuum chamber walls, but additional contributions from the Small Optic Suspension (SOS) towers, for example, could be present.

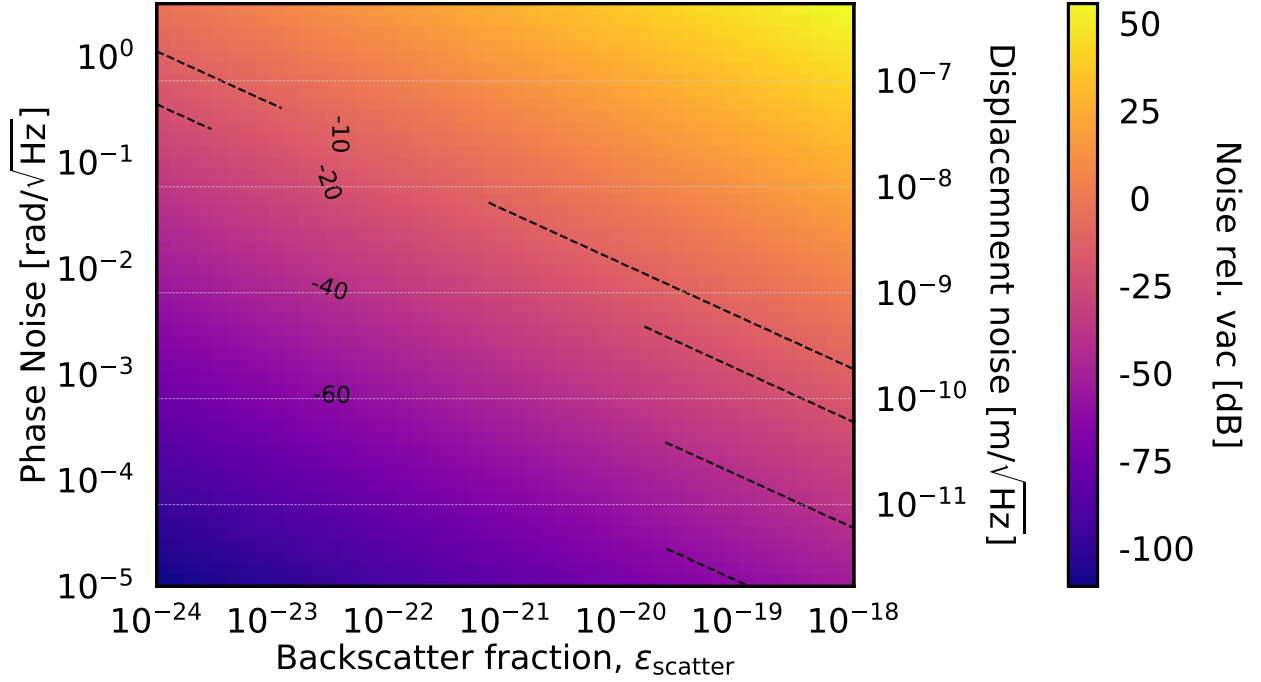


Figure 25: Contribution of phase noise on directly-backscattered light in the readout quadrature defined by $\zeta = 0^\circ$. In this scenario (middle panel of Figure 24), a fraction $\epsilon_{\text{scatter}}$ of the assumed 60 kW of circulating power in the FP arm cavities is directly scattered onto the OMC DCPDs.

3. The solid angle subtended by the OMC DCPDs onto the scattering surface.

Figure 25 shows the calculated contribution of phase noise on the backscattered field to the readout in the quadrature defined by $\zeta = 0^\circ$. Depending on the specific scattering mechanism, quadrature noises on the backscattered field can contribute differently to the readout quadrature (since the phase of the backscattered light relative to the LO field is not controlled). We make the simplistic assumption that any noise on the backscattered field may be divided equally among the two orthogonal quadratures.

7.2 OMC backscatter

Any light in the TEM00 mode of the OMC cavity will be resonant in the cavity. Given that the OMC cavity is a ring cavity, there can be a resonant counter-propagating mode (generated by light scattering out of the forward propagating TEM00 mode of the OMC at the HR mirror surfaces) which leaks out of the OMC's input coupler back to the antisymmetric port of the interferometer. While this field is attenuated by the Output Faraday Isolator (OFI), any noise in either quadrature of the leakage light that makes it back to the interferometer's antisymmetric port will appear as noise additional to the squeezed/unsqueezed vacuum. It has been demonstrated that the total fraction of backscattered light from this path (after accounting for the OFI) is at the level of 10 ppm. This analysis neglects the scatter of carrier HOM light back into the TEM00 mode at the incident mirror of the OMC, which is assumed to be much less than the LO field level.

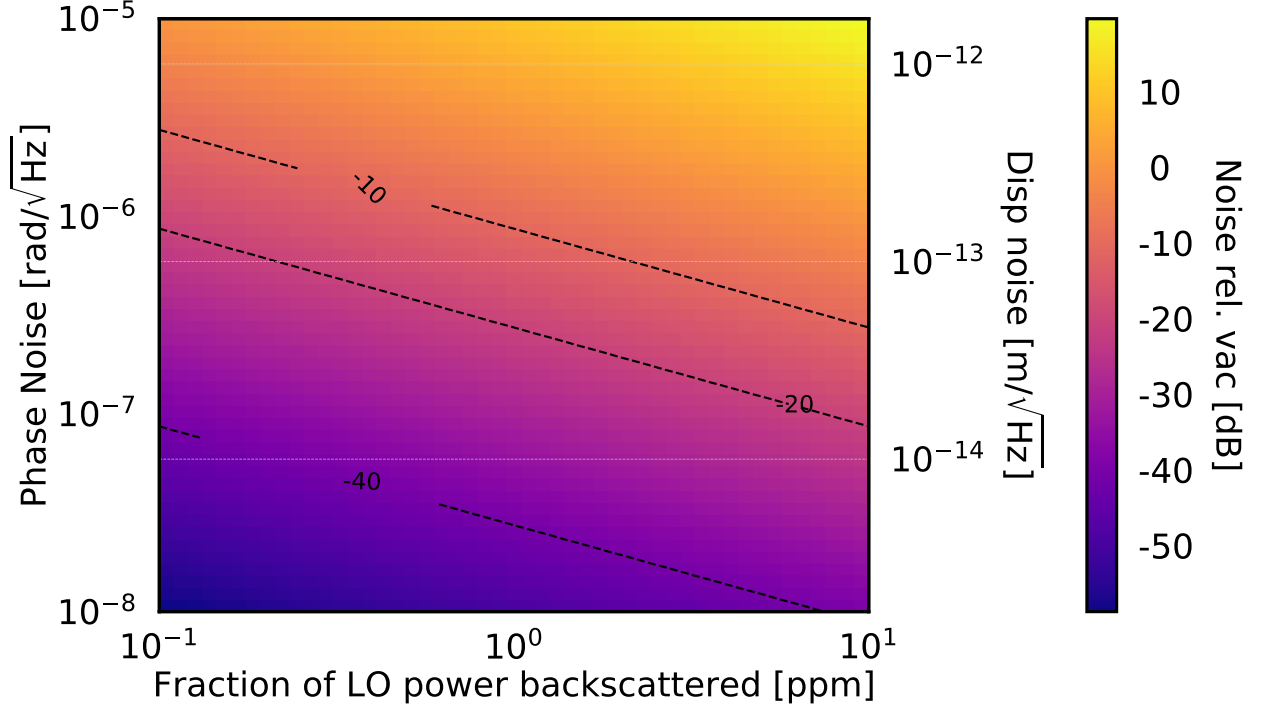


Figure 26: Contribution of quadrature noise as a function of the fraction of incident TEM00 mode light backscattered towards the IFO's antisymmetric port. The quoted fraction includes isolation by the OFI. This is primarily assumed to come from the LO field incident on the OMC cavity becoming resonant in the cavity's counter-propagating mode. The readout quadrature is assumed to be $\zeta = 0^\circ$.

Figure 26 shows the contribution of phase noise on the counterpropagating OMC field in the readout quadrature defined by $\zeta = 0^\circ$. As described in the preceding section, the phase picked up by the scattered light can be random, and hence, may show up in any quadrature relative to the LO (i.e. RIN on this field may also manifest in the $\zeta = 0^\circ$ quadrature). Nevertheless, using this simplistic picture, we can place some limit on the permissible motion of the OMC mirrors (which is assumed to dominate the motion due to the actual OMC suspension due to the amplification of phase noise by the resonant OMC cavity). Any length noise in the OMC will introduce a phase noise that is enhanced by the cavity. According to Fig. 22 at 100 Hz the thermal motion of the OMC mirrors is $\sim 5 \times 10^{-17} \text{m}/\sqrt{\text{Hz}}$. According to Fig. 26 the phase noise induced by the OMC length noise is enhanced by a factor of $\sim 10^2$ to a level of $\sim 10^{-7} \text{rad}/\sqrt{\text{Hz}}$. This means that for a back-scattered light of 10ppm of LO beam from the OMC the induced noise is more than 20db below the vacuum level.

8 Downstream loss requirements

Any optical losses between the interferometer and the readout photodiodes will couple some amount of unsqueezed vacuum into the readout quadrature. In order to be able to measure below the level of the unsqueezed vacuum state, this coupling must be kept sufficiently small. In this section, some sources of optical loss are discussed, and requirements on the amount of loss that can be tolerated are specified.

8.1 Photodiode quantum efficiency

State-of-the-art InGaAs photodiodes with an active area of 3 mm have been demonstrated to have a quantum efficiency $\geq 98\%$ (after undergoing vacuum compatibility procedures and installation). While some techniques have been proposed to increase the effective quantum efficiency further, we conservatively budget **2%** loss in the detection photodiodes. A detailed discussion of the sources of quantum inefficiency in detection photodiodes may be found in [\(cite something here\)](#).

8.2 Output Faraday isolator

An [OFI](#) will be required between the interferometer's antisymmetric port and the [BHD](#) setup, in order to attenuate the amount of back-scattered light. There will be some amount of optical losses associated with this element. For the planned 40m upgrade, we anticipate using a commercial Faraday isolator that suffers **2%** loss single-pass. This is a more relaxed requirement compared to the 1% loss required by the specifications for the A+ low loss Faraday isolator [2].

8.3 Super-polished HR routing mirrors

Some loss will be incurred due to transmission through the mirrors that route the signal field from the interferometer's antisymmetric port to the [BHD](#) setup. Additionally, a small fraction of light will also need to be picked off for angular control, [RF](#) locking of the interferometer, and other diagnostic purposes. We budget **1%** loss for these purposes. This assumes five steering optics each with a loss 50 ppm, a 1000 ppm pickoff for [RF](#) locking, and a 0.75% pickoff for [Quadrant Photodiode \(QPD\)](#) control.

8.4 OMC losses

Optical losses internal to the $\mathcal{F} = 400$ [OMC](#) cavities will lead to non-unity transmission. We adopt the same requirement on the [OMC](#) transmissivity as the aLIGO [OMC](#), namely that the transmissivity be greater than 98% [6]. Therefore, we budget **2%** loss from the optical losses due to the [OMC](#) mirrors.

8.5 Mode-matching losses

The sum of the optical losses described in the previous subsections will define the total amount of loss that is permissible due to mode-mismatch, η , between the interferometer output mode and the [OMC](#)'s TEM00 mode. In this simplistic analysis, we neglect possible coherent effects due to mode-mismatches between multiple cavities in the interferometer. In order to be able to measure a squeezed state that is 3 dB below the vacuum level for an interferometer with the planned 40m parameters, after taking into account other classical noise sources, we require that the total downstream loss be less than 10%. Hence, we require that $\eta \leq \mathbf{3\%}$. For the planned operating configuration of A+ with 6 dB injected frequency dependent squeezed vacuum, the requirement may be more relaxed at $\eta \leq 10\%$ [\(need to cite a reference here\)](#).

9 Beamsplitter requirements

This section addresses the requirements on the beamsplitters in the BHD setup (shown in Figure 1). There are three beamsplitters to consider: the homodyne beamsplitter which combines the LO and IFO fields and the two output beamsplitters downstream of the OMC cavities. In the first section, we examine the effect of a Transmittance-Reflectivity (T-R) imbalance on the intensity and phase noise requirements of the LO to determine the required balancing and tolerance. In the second section, we consider displacement noise of the beamsplitters to obtain their seismic isolation requirement.

9.1 Transmittance-reflectivity balancing

We first examine the effect of a T-R imbalance of the homodyne beamsplitter on the coupling of LO intensity and phase noise. From this analysis we determine the required T-R balancing and tolerance. We do not consider the two output beamsplitters downstream of the OMC cavities, since we are only interested in their common-mode signals which are not affected by an imbalance.

Assuming a contrast defect of 1 mW and a safety factor of 10, Figure 27a shows the required LO intensity noise as a function of homodyne angle and beamsplitter transmittance. As expected, the optimal splitting ratio for a zero homodyne angle (phase quadrature readout) is exactly 50:50. The best intensity stabilization demonstrated by Advanced LIGO, $2 \times 10^{-9}/\sqrt{\text{Hz}}$, allows for a beamsplitting imbalance of $\pm 10\%$.

For completeness, Figure 27b also shows the required LO phase noise as a function of homodyne angle and beamsplitter transmittance. It can be seen that for every homodyne angle, the requirement is almost independent of the splitting ratio.

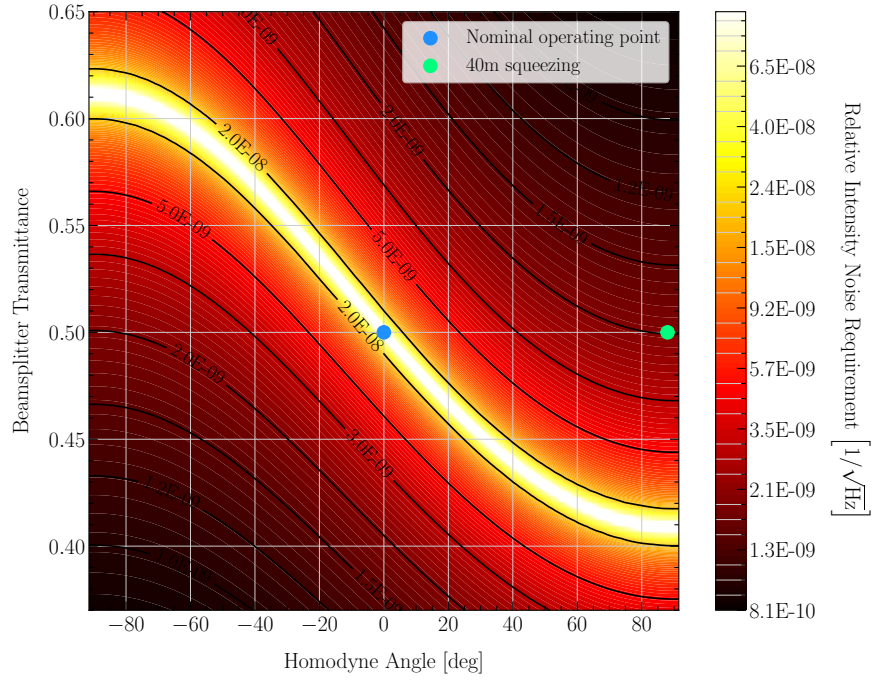
Unexpectedly, for all other homodyne angles, the optimal splitting ratio is not 50:50. For non-zero homodyne angles, this raises the intriguing possibility of using the beamsplitting imbalance to suppress the intensity noise coupling, without worsening the phase noise coupling. Further discussion and an analytic calculation confirming this result are in Appendix C.1.

9.2 Seismic isolation

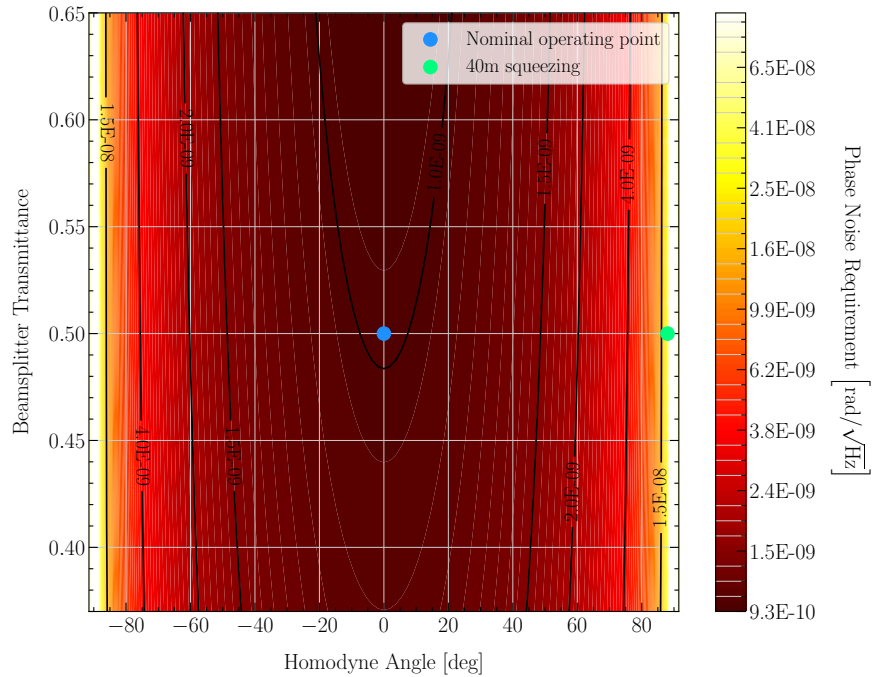
Seismic vibration causes displacement noise on the beamsplitters. This has two effects: First, a relative phase noise between the LO and IFO. Since the beamsplitter is at 45° to these beams, the optical length change is $\sqrt{2}$ times the displacement. Second, the displacement causes a relative lateral shift between the LO and IFO beams. However, this effect is negligible compared to the first effect. We confirm this using a Finesse model.

Therefore, the requirement on the homodyne beamsplitter displacement is essentially the same as the requirement on the LO phase divided by $\sqrt{2}$. In terms of distance, the homodyne beamsplitter is required to be stable to the level of $1.2 \times 10^{-16} \text{ m}/\sqrt{\text{Hz}}$ and $3.5 \times 10^{-15} \text{ m}/\sqrt{\text{Hz}}$ for the phase and amplitude quadrature readouts respectively.

Again, we do not consider the two output beamsplitters downstream of the OMC cavities since their displacement has negligible effect on the detected power.



(a)



(b)

Figure 27: Requirement on T-R imbalance of the homodyne beamsplitter. The intensity (a) and phase (b) noise requirements of the LO are shown as a function of homodyne angle and beamsplitter transmission. An increase in transmittance is compensated by a comensurate decrease in reflectivity, and vice versa, assuming a fixed loss of 100 ppm. For a zero homodyne angle (phase quadrature readout), the required balancing and tolerance is $50 \pm 10\%$.

10 Photodetector requirements

The BHD setup as described requires four photodetectors, one at each of the two output ports of the two output beamsplitters (A and B). The diode current in the relevant channel for readout, the “GW channel”, is formed by the following combination of the currents at the photodetectors

$$i_{\text{GW}} = (i_{A_1} + i_{A_2}) - (i_{B_1} + i_{B_2}). \quad (15)$$

The first two subsections address the noise requirements of each photodetector individually. Two factors are considered here:

1. The input-referred current noise must be at least a factor of 10 lower than shot noise.
2. The amplified voltage signal must be at least a factor of 10 larger than the thermal Johnson noise.

The final subsection then considers the gain-balancing requirements between all four photodetectors together.

10.1 Amplifier noise

To be a factor of 10 below shot noise (i_s), the current noise referred to the input of the transimpedance amplifier must be

$$i_n \leq \frac{i_s}{10} = \frac{\sqrt{2eI}}{10} \quad (16)$$

where $I = \mathcal{E}P_{\text{LO}}/4 = 20 \text{ mA}$, since $P_{\text{LO}} = 100 \text{ mW}$ is the expected LO power and $\mathcal{E} = 0.8 \text{ A/W}$ is the photodiode conversion factor. This gives us an amplifier noise requirement of $i_n \leq 8.0 \times 10^{-12} \text{ A}/\sqrt{\text{Hz}}$. More generally, the requirement can be expressed as

$$i_n \leq \left(8.0 \times 10^{-12} \text{ A}/\sqrt{\text{Hz}}\right) \times \sqrt{\frac{P_{\text{LO}}}{100 \text{ mW}}} \quad (17)$$

for variable LO power.

10.2 Transimpedance gain

The transimpedance gain must be chosen such that the amplified signal is much larger than the thermal Johnson noise of the feedback resistor. Johnson noise is given by $V_{th} = \sqrt{4k_B T R}$, where R is the transimpedance gain and $T = 300 \text{ K}$ is the temperature. Requiring the Johnson noise be factor of 10 below the voltage spectral density of shot noise yields the requirement

$$R \geq \frac{800k_B T}{e\mathcal{E}P_{\text{LO}}} = (259 \text{ } \Omega) \times \frac{P_{\text{LO}}}{100 \text{ mW}}. \quad (18)$$

For the expected LO power of 100 mW, the transimpedance gain requirement is $R \geq 260 \text{ } \Omega$. However, since it is not currently known what the actual experimentally achievable LO power at the 40m will be, it is advisable to place the photodetector electronics outside the vacuum to be able to change this resistor and other relevant components.

10.3 Transimpedance gain balancing

While the GW-channel signal given by Equation (15) is expected, in actuality there may be imbalances that decrease the common mode rejection. Although an imbalance can arise from differences in quantum efficiency, transimpedance amplifier gain, and others, the imbalance is modeled in terms of unitless effective gains. Incorporating the effective gains $\alpha_{1,2}$ and $\beta_{1,2}$, the GW-channel signal is modified as

$$i_{\text{GW}} = (\alpha_1 i_{A_1} + \alpha_2 i_{A_2}) - (\beta_1 i_{B_1} + \beta_2 i_{B_2}) . \quad (19)$$

Before subtraction, digital gains $A_{1,2}$ and $B_{1,2}$ can be applied to correct for this according to the measured values of $\alpha_{1,2}$ and $\beta_{1,2}$. Thus, the compensated GW-channel signal is

$$i_{\text{GW}} = \left(\frac{\alpha_1}{A_1} i_{A_1} + \frac{\alpha_2}{A_2} i_{A_2} \right) - \left(\frac{\beta_1}{B_1} i_{B_1} + \frac{\beta_2}{B_2} i_{B_2} \right) . \quad (20)$$

where each of the pre-factors for the photocurrents must be ~ 1 for BHD.

Since the shot noise in the GW channel is $\sqrt{4 \times i_s^2} = 2i_s$, referred to amplifier input, the requirement on common-mode RIN rejection is

$$i_{\text{RIN}} = \left(\frac{\alpha_1}{A_1} + \frac{\alpha_2}{A_2} - \frac{\beta_1}{B_1} - \frac{\beta_2}{B_2} \right) I \mathcal{R} \leq \frac{2i_s}{10} , \quad (21)$$

where \mathcal{R} is the common-mode RIN. In terms of the gain imbalance after digital correction, $G = \left(\frac{\alpha_1}{A_1} + \frac{\alpha_2}{A_2} - \frac{\beta_1}{B_1} - \frac{\beta_2}{B_2} \right)$, this requirement can be written as

$$G \leq (8.0\%) \times \sqrt{\frac{100 \text{ mW}}{P_{\text{LO}}}} \times \left(\frac{10^{-8}/\sqrt{\text{Hz}}}{\mathcal{R}} \right) . \quad (22)$$

For the expected LO power of 100 mW and a technical RIN of $10^{-8}/\sqrt{\text{Hz}}$, the gain balancing requirement is $G \leq 8.0\%$.

A Interferometer contrast defect

A.1 Definitions

An important consideration in several of the calculations presented in this document is the amount of contrast defect light present at the antisymmetric port of the interferometer. This term is confusingly used to refer to several different effects in the LIGO literature. For the purposes of this document, we define the contrast defect, \mathcal{C} , as the ratio of the amount of light leaking to the dark port of the interferometer to the power circulating in the interferometer. Mathematically,

$$\mathcal{C} = \frac{\int_S dS (E_x - E_y)}{\int_S dS (E_x + E_y)}, \quad (23)$$

where the integrals are over the spatial coordinates of the detecting element, while E_x and E_y denote the electric fields from the X and Y arm cavities at the beam splitter. Adding a signal recycling mirror will merely scale this number.

Clearly, there are a number of factors that determine the amount of contrast defect light. These are:

1. Imbalance between the [ITM](#) transmissivities.
2. Imbalance between the [End Test Mass \(ETM\)](#) transmissivities.
3. Imbalance between the round-trip arm cavity loss (finesse imbalance).
4. Imbalance between the reflectivity and transmissivity of the beamsplitter (e.g. due to an [Anti-Reflective \(AR\)](#) coating).
5. Imperfect spatial overlap of the modes from the two arm cavities at the beamsplitter.

The first three collectively result in an asymmetry of the reflectivities of the arm cavities. In the following subsections, we analyze these effects quantitatively. It is evident from Equation (23) that in the absence of any asymmetries between the arm cavities, when the interferometer is locked on a dark fringe, there is no (carrier) light at the antisymmetric port. Moreover, the frequency dependence of a given asymmetry on the interferometer noise is dependent on where the asymmetry enters the system.

A.2 DC analysis

Fluctuations in the [LO](#) field are amplified by the DC contrast defect light. Hence, we would like to know how much asymmetry is permissible such that we end up with less than 1 mW of DC contrast defect light at the antisymmetric port, in the TEM00 mode of the [OMC](#). Let us first consider the first three sources of asymmetry listed in Appendix A.1. We allow the test mass transmissivities and intracavity loss to vary about their nominal value by some realistic amount, and look at the variation in the arm cavity power reflectivity. The results are summarized in Figure 28, while the range of parameters scanned are shown in Figure 29. We conclude that the arm cavity amplitude (power) reflectivity is unlikely to be different by more than 1500 ppm (2 ppm).

MC distribution of arm cavity transmissivity

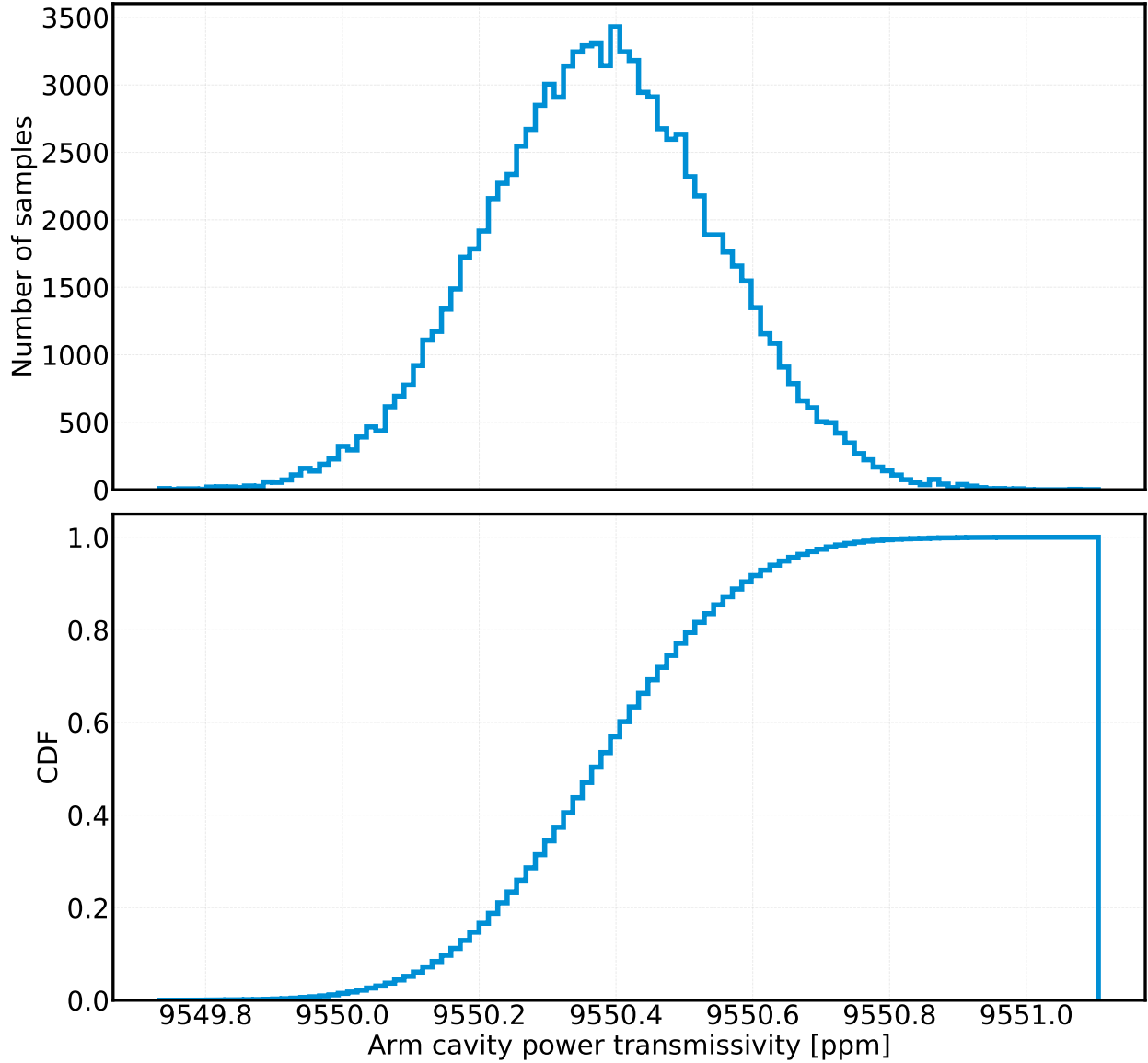


Figure 28: Variation in the arm cavity transmissivity as a result of introducing some asymmetry to the test mass transmissivities and the intracavity loss. Perturbations are applied about the nominal values of these parameters, namely $T_{\text{ITM}} = 1.384\%$, $T_{\text{ETM}} = 13 \text{ ppm}$, $\mathcal{L}_{\text{rt}} = 20 \text{ ppm}$. The distributions of the applied perturbations are shown in Figure 29.

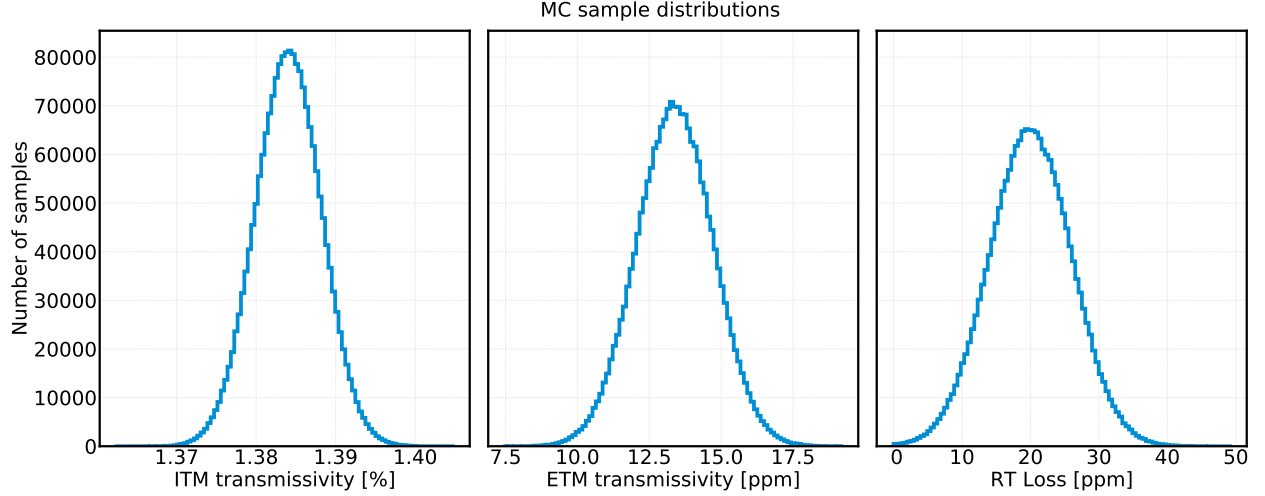


Figure 29: Distribution of the parameters sampled to investigate the effect of asymmetry in the test mass transmissivities and intracavity loss on the arm cavity transmissivity.

To translate this to the amount of light at the antisymmetric port, we need to know the transmissivity from the symmetric port to the antisymmetric port. This is given by

$$t_{\text{DRFPMI}}^{\text{sym} \rightarrow \text{AS}} = \frac{e^{i(\phi_{\text{PRC}} + \phi_{\text{SRC}})} e^{2i\phi_-} (r_X - r_Y) t_{\text{PTs}}}{2e^{2i(\phi_{\text{PRC}} + \phi_{\text{SRC}})} + 2r_{\text{P}} r_{\text{S}} r_X r_Y e^{4i\phi_-} - e^{2i\phi_-} (r_X + r_Y) (r_{\text{S}} e^{2i\phi_{\text{PRC}}} + r_{\text{P}} e^{2i\phi_{\text{SRC}}})} \cdot \quad (24)$$

Here, ϕ_- is the Schnupp asymmetry, while the other symbols should be self evident. The phases ϕ are one-way phases. Since we have the **PRC** resonant for the carrier, and the **Signal Recycling Cavity (SRC)** nearly so, we can simplify the above expression somewhat (for the carrier field) to

$$t_{\text{DRFPMI}}^{\text{sym} \rightarrow \text{AS}} \approx \frac{t_{\text{PTs}} (r_X - r_Y)}{2 + 2r_{\text{P}} r_{\text{S}} r_X r_Y - (r_{\text{P}} + r_{\text{S}}) (r_X + r_Y)} \cdot \quad (25)$$

Figure 30 shows the power transmissivity as a function of the amplitude reflectivity imbalance between the two arm cavities. With 10 W of input power to the interferometer's symmetric port, it is likely that we will have more than 1 mW of contrast defect light at the antisymmetric port due to these sources of asymmetry. If we want to have a larger safety margin, we will have to match the **ITM** transmissivities to $\approx 0.1\%$.

Next, we consider the contribution to the contrast defect from the mismatched **RoCs** of the two **ETMs** (since the 40m **ITMs** are flat). In other words, misalignment effects are neglected. Hence, per [9], we only need to consider the TEM_{02} and TEM_{20} modes (to lowest order). [10] derives the analytic form of this by analyzing the reflectivity of the arm cavity for an input beam whose waist size differs from that of an arm cavity eigenmode (the assumption being that it is perfectly matched to the other arm). We adapt this analysis, incorporating

1. **SRC** cavity gain for the 00 and 02/20 modes.
2. Lossy arm cavities.
3. Complex reflectivities based on Gouy Phase (i.e. fields are not assumed to be exactly resonant / anti-resonant).

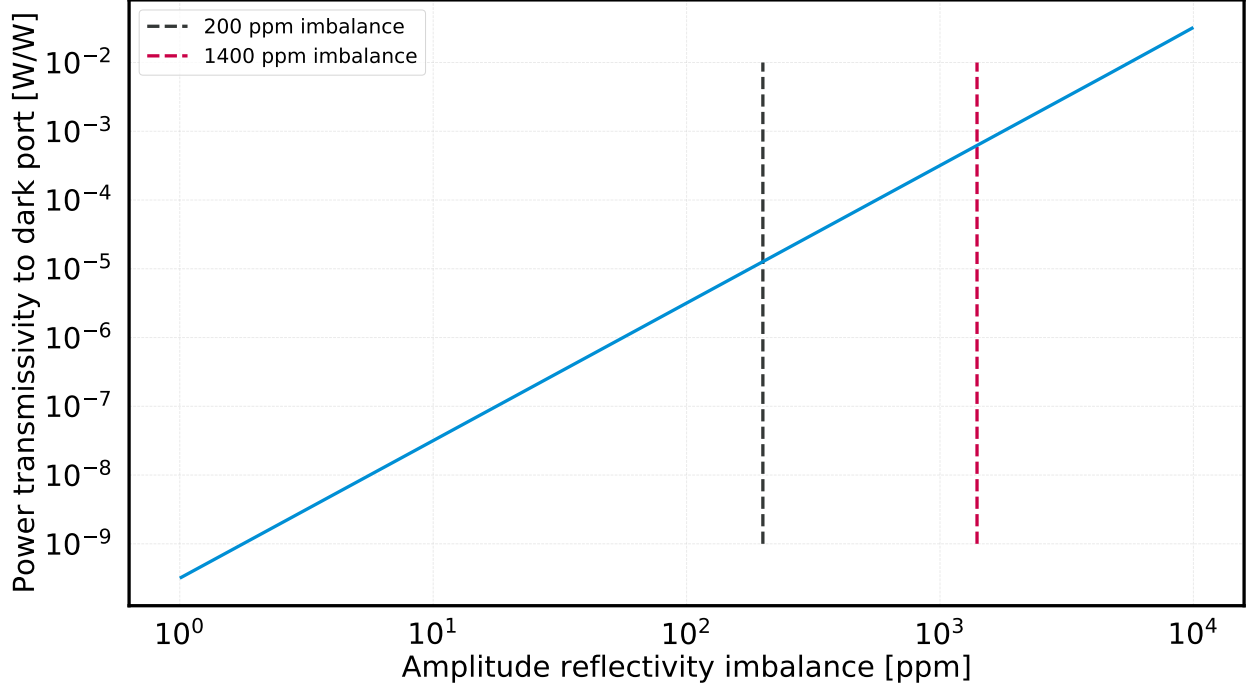


Figure 30: Distribution of the parameters sampled to investigate the effect of asymmetry in the test mass transmissivities and intracavity loss on the arm cavity transmissivity.

The relevant relation for this analysis from [10]:

$$\mathcal{C} = 1 - \frac{2\Re[r_a\alpha_{00}]}{|r_a|^2 + |\alpha_{00}|^2 + 2|\alpha_{02}|^2}, \text{ where } \alpha_{00} \equiv r_a c_{00}^2 + 2\hat{r}_a c_{02}^2, \quad \alpha_{02} \equiv r_a c_{00}c_{02} - \hat{r}_a c_{02}c_{22}. \quad (26)$$

Note the factor of 2 in front of the α_{02} term, which we believe is missing in [10]. We have also accounted for the fact that the matched arm has losses, and so does not have reflectivity of +1 for the TEM₀₀ field.

Actually, for this analysis, we are more interested in the actual amount of power leaking to the dark port when locked on the dark fringe, in the IFO TEM₀₀ mode. The power at the dark port is given by

$$P_{\text{dark}} = g_s^2 P_{\text{in}} \left(\frac{|r_a|^2}{4} + \frac{|\alpha_{00}|^2}{4} - \frac{1}{2} \Re[r_a \alpha_{00}] \right) + \hat{g}_s^2 P_{\text{in}} \left(\frac{|\alpha_{02}|^2}{2} \right), \quad (27)$$

where we have allowed for α terms to be complex. The first term contributing to the TEM₀₀ mode, and the second term being in the TEM₀₂ and TEM₂₀ modes, and g_s , \hat{g}_s signify the mode healing/harming due to the SRC. For a first pass, $r_a = 1$, $\hat{r}_a = -1$ (for a more realistic calculation, we will need to take into account the arm cavity losses and the non-perfect rejection of the $m + n = 2$ mode). Of the contrast defect light, only the TEM₀₀ part will pass through the OMC with high transmission, and hence, contribute to shot noise on the BHD photodetectors (for a first pass, we assume OMC completely rejects the other junk light). The coupling coefficients c_{ij} are given in the appendix of [10]. There are only 3

unique ones, the other coefficients are all related to these three by a sign change. The three relevant ones are

$$c_{00} = \frac{2\omega_0\omega_1}{\omega_0^2 + \omega_1^2}, \quad c_{02} = -\frac{\sqrt{2}\omega_0\omega_1(\omega_0^2 - \omega_1^2)}{(\omega_0^2 + \omega_1^2)^2}, \quad c_{22} = -\frac{\omega_0\omega_1(\omega_0^4 - 10\omega_0^2\omega_1^2 + \omega_1^4)}{(\omega_0^2 + \omega_1^2)^3}, \quad (28)$$

where ω_0 is the input beam waist (assumed to be matched to one of the arms) while ω_1 is that for the other arm.

The last piece is to define the waist size for the TEM₀₀ eigenmode of a linear two-mirror cavity of length L , with mirrors whose RoCs are R_1 and R_2 , given by

$$\omega_0 = \sqrt{\frac{\lambda L}{\pi}} \left(\frac{g_1 g_2 (1 - g_1 g_2)}{(g_1 + g_2 - 2g_1 g_2)^2} \right)^{\frac{1}{4}}, \quad \text{where } g_i = 1 - \frac{L}{R_i}, \quad i = 1, 2. \quad (29)$$

Figure 31 shows the amount of contrast defect, as defined in Equation (26), as a function of the RoC of one of the test masses.

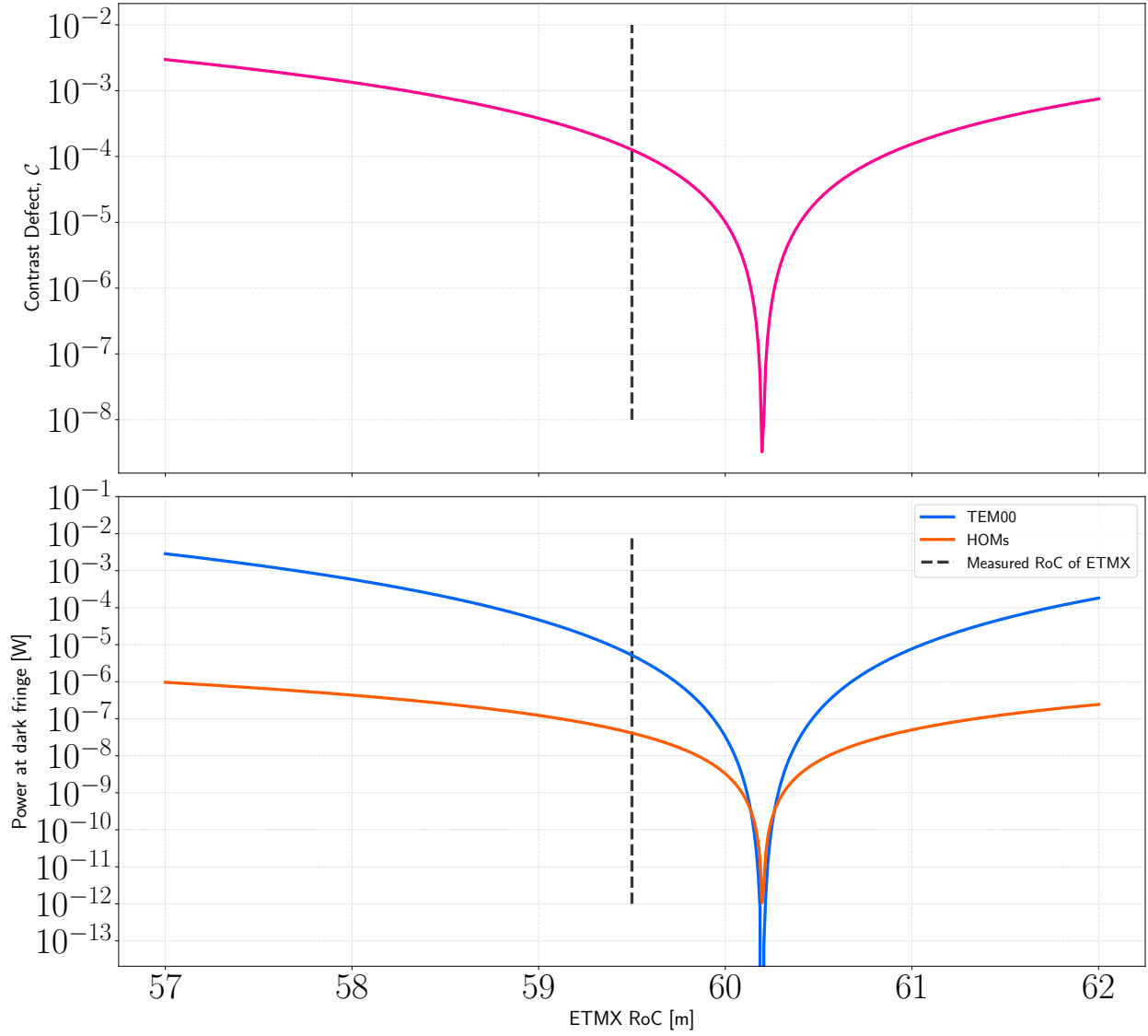


Figure 31: Contrast defect as a function of the RoC.

B OMC optical layout

This is a brief overview of the design thought process.

Why does the OMC have four (and not fewer or more) mirrors? We need at least two mirrors to form an optical cavity. The simplest cavity one can imagine is the linear two mirror cavity. This is not a good choice for the OMC because the amount of backscattered light increases exponentially with smaller angles of incidence. Even with state-of-the-art AR coatings, a linear cavity would result in large backscatter into the IFO Anti-Symmetric (AS) port, which would create additional noise.

The next simplest option is the three-mirror folded cavity, like the Input Mode Cleaner (IMC). However, an optical cavity with an odd number of mirrors has a complicated HOM resonance structure (relative to its even number mirror counterpart). Since one of the purposes of the OMC is to filter out unwanted HOMs, such an extra complication is undesirable. Which brings us to the choice of four-mirror optical cavity where the additional complexity of the HOM resonance structure is avoided.

By having a small but non-zero angle of incidence, θ_i , the direct backscatter can be attenuated, since the BRDF of super-polished mirrors is expected to fall off as $1/\theta_i^2$ (need a citation). Finally, with super-polished mirrors each having optical loss at the level of 5 ppm per bounce for a $500\ \mu\text{m}$ beam, it is possible to have a cavity with a finesse of ≈ 400 for sufficient filtering of unwanted fields, while still achieving $\geq 99\%$ transmission of the DARM signal field.

Having decided on the number of mirrors forming the OMC cavity, the design problem is then to decide the geometry of the cavity, and the power transmissivities of the mirrors. A schematic drawing of the OMC optical layout is shown in Figure 32. For simplicity, we stick to the aLIGO OMC design [6], with two flat mirrors and two curved mirrors. Furthermore, for a start, we preserve the aLIGO OMC choice of cavity finesse, $\mathcal{F} \approx 400$, and angle of incidence, $\theta_i \approx 4^\circ$. The design problem then amounts to the following: what should the values of the parameters L_1 and RoC be, such that the functions outlined in Section 6.1 are satisfied?

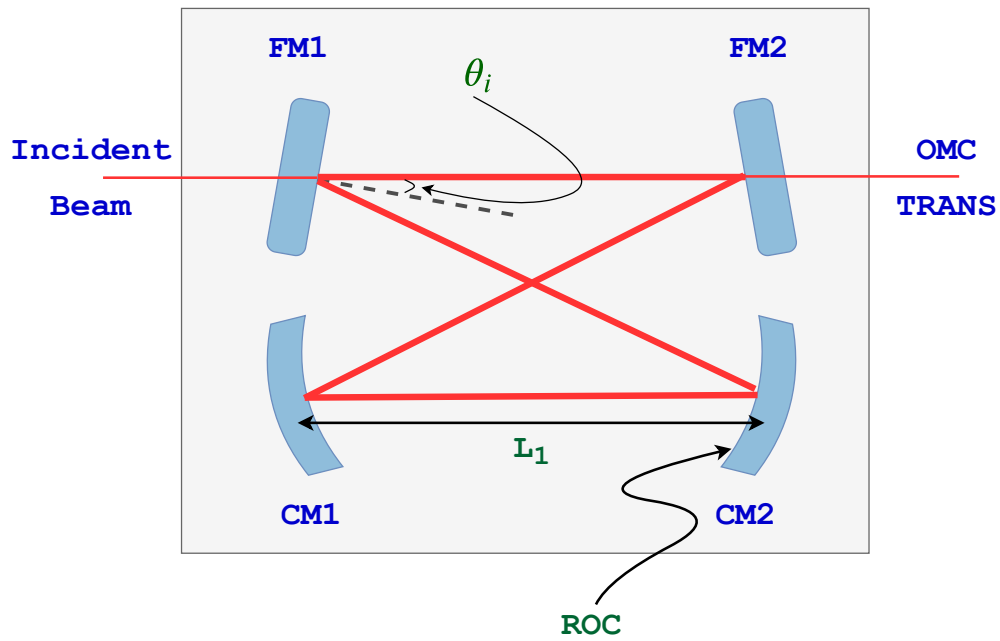


Figure 32: Proposed OMC optical layout. To preserve symmetry, the mirrors labelled FM1 and FM2 are flat, and CM1 and CM2 have identical curvatures. The geometrical design parameters, namely the angle of incidence θ_i , the length L_1 , and the radius of curvature of the curved mirrors, ROC, are indicated in green. In addition to these, the OMC design has to determine the power transmissivities of the FMs, t_F^2 and CMs, t_C^2 .

C 40m ponderomotive squeezing

The planned 40m ponderomotive squeezing experiment is expected to generate an interferometer output field that is a few dB below unsqueezed vacuum. Therefore, the realized **BHD** system should be able to detect a squeezed state that is 6 dB below unsqueezed vacuum between 100 Hz — 1 kHz, with all noises associated with the **BHD** system a safety factor of 10 below the next highest noise source in the **DARM** noise budget in the target frequency band. The ponderomotive squeezing is expected to be maximum in a quadrature that is close to the amplitude quadrature, and hence, for this case study, we expect the homodyne angle to be in the range $\zeta \approx 80^\circ - 90^\circ$. For modeling purposes we assume a value $\zeta = 88^\circ$.

C.1 Beamsplitter imbalance analytic calculation

To analytically understand the effect of an imbalance, we generalize the calculation of Steinlechner et al. [4] for arbitrary transmission and reflection coefficients, t and r , respectively (in [4] the coefficients are fixed to $r^2 = t^2 = 0.5$). For simplicity we define the coefficients such that $t^2 + r^2 = 1$ (i.e., losses are neglected). We adopt the same notation as in [4] for ease of comparison.

The **LO** field, \mathbf{a} , and signal field, \mathbf{b} are incident on the beamsplitter as shown in Figure 33. For arbitrary t and r coefficients, the fields at the two output ports are

$$\mathbf{c} = t\mathbf{a}e^{i\phi} + r\mathbf{b} \quad (30)$$

$$\mathbf{d} = -r\mathbf{a}e^{i\phi} + t\mathbf{b} . \quad (31)$$

The photon number operators (proportional to power) at the output ports are then

$$\mathbf{c}^\dagger \mathbf{c} = t^2 \mathbf{a}^\dagger \mathbf{a} + r^2 \mathbf{b}^\dagger \mathbf{b} + rt (\mathbf{a}^\dagger \mathbf{b}e^{-i\phi} + \mathbf{b}^\dagger \mathbf{a}e^{i\phi}) \quad (32)$$

$$\mathbf{d}^\dagger \mathbf{d} = r^2 \mathbf{a}^\dagger \mathbf{a} + t^2 \mathbf{b}^\dagger \mathbf{b} - rt (\mathbf{a}^\dagger \mathbf{b}e^{-i\phi} + \mathbf{b}^\dagger \mathbf{a}e^{i\phi}) . \quad (33)$$

Following [4], we decompose the **LO** field as $\mathbf{a} = \alpha + \delta\mathbf{a}$, where α is the classical (average) field amplitude and $\delta\mathbf{a}$ is a quantum perturbation. We analogously decompose the signal field as $\mathbf{b} = \beta + \delta\mathbf{b}$. To first order in the perturbations, the output-port intensities can be rewritten as

$$\mathbf{c}^\dagger \mathbf{c} = t^2 (\alpha^2 + 2\alpha\delta\mathbf{X}_1^a) + r^2 (\beta^2 + 2\beta\delta\mathbf{X}_1^b) + rt (2\alpha\beta \cos \phi + 2\alpha\delta\mathbf{X}_\phi^b + 2\beta\delta\mathbf{X}_{-\phi}^a) \quad (34)$$

$$\mathbf{d}^\dagger \mathbf{d} = r^2 (\alpha^2 + 2\alpha\delta\mathbf{X}_1^a) + t^2 (\beta^2 + 2\beta\delta\mathbf{X}_1^b) - rt (2\alpha\beta \cos \phi + 2\alpha\delta\mathbf{X}_\phi^b + 2\beta\delta\mathbf{X}_{-\phi}^a) , \quad (35)$$

where $\delta\mathbf{X}_1^a = (\delta\mathbf{a} + \delta\mathbf{a}^\dagger)/2$, $\delta\mathbf{X}_2^a = -i(\delta\mathbf{a} - \delta\mathbf{a}^\dagger)/2$, and $\delta\mathbf{X}_\phi = \delta\mathbf{X}_1 \cos \phi + \delta\mathbf{X}_2 \sin \phi$ are the amplitude, phase, and ϕ quadrature operators, respectively. Note that the notation of [4] uses the opposite phase convention of this work (i.e., $\phi = 0^\circ$ is the *amplitude* quadrature). The two conventions are related by $\phi = 90^\circ - \zeta$.

The differential photocurrent measured between the two output ports is proportional to the difference in the incident number of photons,

$$\begin{aligned} \mathbf{i}_- &= \mathbf{c}^\dagger \mathbf{c} - \mathbf{d}^\dagger \mathbf{d} \\ &= 4rt (\alpha\beta \cos \phi + \alpha\delta\mathbf{X}_\phi^b + \beta\delta\mathbf{X}_{-\phi}^a) + (t^2 - r^2) (\alpha^2 - \beta^2 + 2\alpha\delta\mathbf{X}_1^a - 2\beta\delta\mathbf{X}_1^b) \\ &= 2\sqrt{1 - \epsilon^2} (\alpha\beta \cos \phi + \alpha\delta\mathbf{X}_\phi^b + \beta\delta\mathbf{X}_{-\phi}^a) + \epsilon (\alpha^2 - \beta^2 + 2\alpha\delta\mathbf{X}_1^a - 2\beta\delta\mathbf{X}_1^b) , \end{aligned} \quad (36)$$

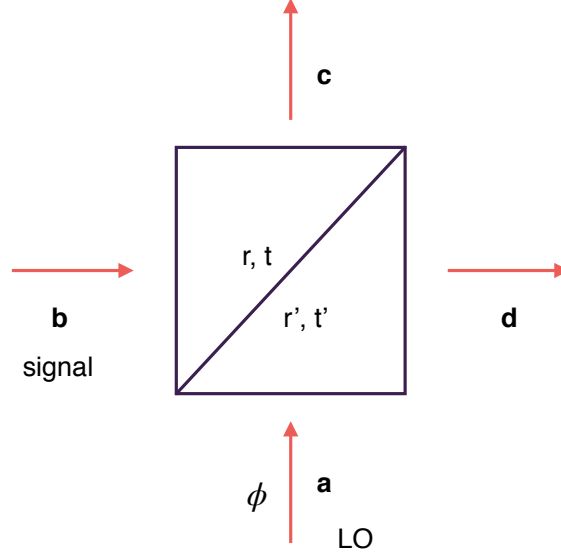


Figure 33: Imbalanced beamsplitter

where in the final line we have defined the beamsplitter imbalance $\epsilon = t^2 - r^2$ and used the fact that $t^2 + r^2 = 1$. Neglecting covariance between the **LO** and signal fields, and between the amplitude and phase quadratures of an individual field, the noise variance of Equation 36 is

$$\begin{aligned} \Delta^2 \mathbf{i}_- = & 4(1 - \epsilon^2) (\alpha^2 \Delta^2 \delta \mathbf{X}_\phi^b + \beta^2 \Delta^2 \delta \mathbf{X}_{-\phi}^a) + 4\epsilon^2 (\alpha^2 \Delta^2 \delta \mathbf{X}_1^a + \beta^2 \Delta^2 \delta \mathbf{X}_1^b) \\ & + 8\epsilon \sqrt{1 - \epsilon^2} \alpha \beta \cos(\phi) (\Delta^2 \delta \mathbf{X}_1^a - \Delta^2 \delta \mathbf{X}_1^b) . \end{aligned} \quad (37)$$

We make several observations about this result:

1. For the balanced case ($\epsilon = 0$), the second and third terms vanish, and Equation 37 reduces to Equation 5 of [4].
2. The second term is always ≥ 0 , so can only increase the noise variance.
3. The third term can be positive or negative. For fixed ϕ and input field noise variances, the sign of this term can be inverted by changing the beamsplitter imbalance $\epsilon \rightarrow -\epsilon$. In general, this can be used to *partially offset* the **LO** amplitude noise coupled through the first term.
4. If the amplitude noise variances are equal ($\Delta^2 \delta \mathbf{X}_1^a \approx \Delta^2 \delta \mathbf{X}_1^b$), then the third term vanishes and a beamsplitter imbalance can only increase the noise variance.
5. Similarly, if the readout is in the phase quadrature ($\phi = 90^\circ$), then the third term again vanishes and a beamsplitter imbalance can only increase the noise variance.

From the above, it is clear that a **T-R** imbalance in the homodyne beamsplitter can only degrade the noise performance for phase-quadrature readout. However, it can offer a significant reduction in the **LO RIN** requirement for the ponderomotive squeezing case, which will

be operated $\sim 2^\circ$ from the amplitude quadrature. To illustrate this, we consider the case of readout in the amplitude quadrature ($\phi = 0^\circ$). In this case the noise variance is

$$\begin{aligned} \Delta^2 \mathbf{i}_-^{\phi=0^\circ} = & 4(1 - \epsilon^2) (\alpha^2 \Delta^2 \delta \mathbf{X}_1^b + \beta^2 \Delta^2 \delta \mathbf{X}_1^a) + 4\epsilon^2 (\alpha^2 \Delta^2 \delta \mathbf{X}_1^a + \beta^2 \Delta^2 \delta \mathbf{X}_1^b) \\ & + 8\epsilon\sqrt{1 - \epsilon^2} \alpha\beta (\Delta^2 \delta \mathbf{X}_1^a - \Delta^2 \delta \mathbf{X}_1^b) . \end{aligned} \quad (38)$$

Expanding Equation 38 to first order in the imbalance $\epsilon < 1$ and collecting terms,

$$\Delta^2 \mathbf{i}_-^{\phi=0^\circ} = (4\alpha^2 - 8\epsilon\alpha\beta) \Delta^2 \delta \mathbf{X}_1^b + (4\beta^2 + 8\epsilon\alpha\beta) \Delta^2 \delta \mathbf{X}_1^a + O(\epsilon^2) . \quad (39)$$

Thus it is clear that, to leading order, there exists an imbalance $\epsilon = -\beta/(2\alpha)$ which *zeros* the amplitude noise coupling of the LO while slightly enhancing the signal field coupling.

Finally, we note that an analogous effect can be achieved through the selective unbalancing of the BHD photodetector gains. This is the easier implementation in practice, as the photodetector gains can be variably tuned outside the vacuum.

D 40m BHD testing plan

D.1 Lock acquisition

Here we test the transition sequence to change the DARM readout from the RF signal to the BHD signal. Specifically, we test the following (in the order of a potential locking sequence; assumed the IFO have locked with RF DARM):

- Alignment of the LO beam. Dither the LMs (steering mirrors for the LO path) in angle and demodulate the OMCs' transmitted power. Move the LMs in angle to zero this signal and check if it corresponds to the maximum of the OMCs' transmitted power. Also check the SNR of this alignment signal relative to ambient noise.
- Initial alignment of the AS beam. First introduce offsets in DARM to make a bright AS beam, and align the AS path in a way similar to the LO path. Specifically, dither the OMs (steering mirrors for the AS path) at an AC frequency and move the DC alignment of the OMs to zero the demodulated signal read out at the OMC transmission.
- Alignment of the AS beam without DARM offset. Once the initial alignment of the AS path is done, remove the DARM offset. Then there are a few possibilities of maintain the AS path's alignment.

1). The simplest one is to record the beam's position on DC QPDs on the OMCs reflection, and then lock the alignment to those DC positions. The drawback of this scheme is that the locking point can be easily contaminated by carrier junk lights which may drift in long term. If the drift is significant, then the DC QPDs can only be AC coupled to stabilize some AC seismic motion.

2). The next possibility is to dither the AS mirrors and demodulate the power on the OMCs reflection. This relies on the interference between the f2 field from the AS with the f2 from the LO. Since both are RF sidebands, they experience different mode content as the main carrier field.

3). One can also dither differential ETMs and demodulate the SUM channel (sum of the PDs on the OMCs' transmission) as the error signals for the OMs' alignment. This scheme might be contaminated by the common ETM residual RMS.

4). Lastly, dither both DARM in length and the OMs in angle, and form error signals for the OMs by demodulating DARM readout at the beat note frequencies between the longitudinal and angular dithering. This should be the least contaminated signal by other defect. However, it also has the worst sensitivity as double dithering is required.

We will measure the response of each error signal relative to ambient noise. To check if the zero point is reasonable, should also dither DARM in length and measure the BHD DARM response. For each alignment scheme, the zero crossing should corresponds to the maximum of the DARM response.

- OMC locking. Test if we can have both OMC stably locked using aLIGO-like dithering scheme with the bright LO field.
- Homodyne angle ζ . Dither both DARM and the LO path in length and demodulate the BHD DARM at the beat note frequency to form an error signal for the LO angle control. Then introduce DC offsets in the LO angle and measure the response of this error signal. Compare the signal response to the ambient noise to determine if extra AC stabilization is required.

If an RF PD at $(f_2 - f_1)$ frequency will be available, can also check the zero crossing of this signal with respect to the double-dithering scheme. May either DC couple this signal with an offset determined by the double-dithering scheme, or only AC couple this signal.

- Once all the DC locking points are set, transition DARM readout from RF readout to BHD readout. Check if the lock can be maintained stably, or if extra stabilizations for certain BHD DOFs is required.
- Measure the DARM optical response locked with BHD readout and compare it with the measurement when DARM is locked using RF. Test if the transfer functions are consistent with each other.

D.2 Noise couplings

The noise requirements described in this document were calculated using idealized models and estimates. To be certain that our requirements are truly met, measurements of the real noise couplings are needed. These measurements will be done in a way similar to the way they were calculated: once the degrees of freedom of IFO + BHD are locked, noise and/or offsets will be measured/induced at one point, while noise is being measured in another point. In that way, we will deduce the real noise couplings.

Some of these couplings are actually bi-linear in nature. The unavoidable RMS detunings - effectively DC offsets - of the noisy degrees of freedom can couple AC noise into the readout. It will also be important to measure these RMS detunings.

- Measure the coupling of length noise of the OMC to the readout by applying both DC and AC signals to the OMC PZTs and measure the readout at the same AC frequency.

The measurement can then be used to estimate the nominal OMC noise projection by replacing the DC term with the residual RMS and the AC term the spectrum of the OMC length noise (e.g., thermal and accoustic).

- Scattered light noise. Measure the light at the reflected light port of the Faraday isolator. This port is distinct from the OMCs' reflected light and is a measure of the light that is counter propagating in the OMCs. From that measurement we can estimate the light level that is reflected back into the IFO. A scheme for measuring the phase noise due to the phase gain of the OMC will need to be developed.
- Measure the coupling of angular noise of the steering mirrors into the readout by by applying both DC and AC signal to the steering mirror's coil drivers and measure the readout at the same AC frequency. This can be used to project the nominal noise coupling by replacing the DC term with the RMS motion of the steering mirror and the AC term the angular spectra of the steering mirrors (seismic motion times suspension transfer function).
- Measure the coupling of angular noise of the IFO mirrors to the readout by introducing DC offsets on the steering mirrors. Then replace the DC offset by the RMS motions of the steering mirrors to project the nominal noise coupling.
- Measure the coupling of RIN to the readout by intentionally unbalancing the BHD PD gains and by offsetting homodyne angle.
- Measure the LO phase noise by injecting AC signals to the homodyne angle and measure the readout at the injection frequencies.
- From the coupling strength of the LO phase noise to the readout measure the leakage of the carrier TEM_{00} field into the AS port due to differential losses of the ARM cavities. (Note this is different from the contrast defect measurement, as the contrast defect is usually dominated by $TEM_{02/20}$ modes generated by differential mode-matching. A $TEM_{02/20}$ field does not couple with the LO phase noise due to the spatial orthogonality). This measurement will be compared to a direct measurement of the differential arm loss using cavity ringdowns or other loss measurement techniques. Such a direct measurement will be done in the near future.

D.3 Other tests

Tests that do not require the IFO to be in its final low-noise state.

- Mode matching. Lock DARM with RF and then use the BHD OMCs to do mode scanning of both the LO beam and the AS beam. Derive the mode-matching between both the main IFO and (one of) the OMC, and the mode matching between the two OMCs.
- BHD board internal misalignment. Dither the LMs (steering mirrors for the LO path) in angle and demodulate the OMCs' transmitted power. Then move the LMs in angle to zero the demodulated signal. Check if the zero crossing happens at the same location for the two OMCs. If not, calibrate the difference in the zero crossing location into the BHD BS's misalignment.

- Electronics. Measure the input-referred amplifier noise of the BHD PDs and characterize the response (transimpedance function) of the BHD PDs.
- Suspension assembly tests. These tests involve driving the coil that actuate the mirrors' degrees of freedom and testing for expected signals on the optical shadow sensors.
- OMC optical testings. Measurements of the OMCs' transfer functions, optical losses, FSR, transverse, mode spacing and other tests [11] will be performed to verify their design specifications.

Acronyms

ALS Arm Length Stabilization.

AR Anti-Reflective.

AS Anti-Symmetric.

BHD Balanced Homodyne Readout.

BRDF Bi-directional Reflectance Distribution Function.

DAC Digital to Analog Converter.

DARM Differential Arm Motion.

DCPD DC Photo-Detectors.

ETM End Test Mass.

FEA Finite Element Analysis.

FP Fabry-Perot.

HOM Higher-Order Mode.

HOMs Higher Order Modes.

HR High-Reflectivity.

IFO Interferometer.

IMC Input Mode Cleaner.

ISC Instrument Sensing and Control.

ITM Input Test Mass.

LO Local Oscillator.

OFI Output Faraday Isolator.

OMC Output Mode Cleaner.

Oplev Optical Lever.

PRC Power Recycling Cavity.

PRG Power Recycling Gain.

PZT Piezoelectric Transducer.

QPD Quadrant Photodiode.

RF Radio Frequency.

RIN Relative Intensity Noise.

RMS Root-Mean-Square.

RoC Radius of Curvature.

RSE Resonant Sideband Extraction.

SOS Small Optic Suspension.

SRC Signal Recycling Cavity.

T-R Transmittance-Reflectivity.

VOPO Vacuum Optical Parametric Oscillator.

References

- [1] Alessandra Buonanno and Yanbei Chen. Quantum noise in second generation, signal-recycled laser interferometric gravitational-wave detectors. Phys. Rev. D, 64:042006, Jul 2001.
- [2] Lisa Barsotti, Koji Arai, Aidan Brooks, and Peter Fritschel. Design requirement document of a+ low loss faraday isolators. LIGO Technical Document T1800398, Available at <https://dcc.ligo.org/T1800398> (2018).
- [3] Hang Yu. BHD ISC. LIGO Technical Document G1802014, Available at <https://dcc.ligo.org/LIGO-G1802014> (2018).
- [4] Sebastian Steinlechner, Bryan W. Barr, Angus S. Bell, Stefan L. Danilishin, Andreas Gläfke, Christian Gräf, Jan-Simon Hennig, E. Alasdair Houston, Sabina H. Huttner, Sean S. Leavey, Daniela Pascucci, Borja Sorazu, Andrew Spencer, Kenneth A. Strain, Jennifer Wright, and Stefan Hild. Local-oscillator noise coupling in balanced homodyne readout for advanced gravitational wave detectors. Phys. Rev. D, 92:072009, Oct 2015.
- [5] Joseph Giaime, Partha Saha, David Shoemaker, and Lisa Sievers. A passive vibration isolation stack for ligo: Design, modeling, and testing. Review of Scientific Instruments, 67(1):208–214, 1996.
- [6] Koji Arai, Sam Barnum, Peter Fritschel, Jeffrey Lewis, and Sam Waldman. Output mode cleaner (omc) design. LIGO Technical Document T1000276, Available at <https://dcc.ligo.org/T1000276/public> (2010).
- [7] S Gras, H Yu, W Yam, D Martynov, and M Evans. Audio-band coating thermal noise measurement for Advanced LIGO with a multimode optical resonator. Physical Review D, 95(2):022001–11, January 2017.
- [8] Y Levin. Internal thermal noise in the LIGO test masses: A direct approach. Physical Review D, January 1998.
- [9] Dana Z. Anderson. Alignment of resonant optical cavities. Appl. Opt., 23(17):2944–2949, Sep 1984.
- [10] Koji Arai. Effect of the end mirror curvature error to the contrast of a fabry-perot based michelson interferometer. LIGO Technical Document T1000543, Available at <https://dcc.ligo.org/T1000543/public> (2010).
- [11] Koji Arai, Jeffery Lewis, and William Z. Korth. aligo output mode cleaner: Optical testing and results. LIGO Technical Document T1500060, Available at <https://dcc.ligo.org/LIGO-T1500060> (2017).